Research on Engineering Structures & Materials
www.jresm.org
Research Group

Research Article

Enhancing seismic resilience of tier III/IV data centers: A comparative performance-based evaluation of fixed base and DCFP isolated structures

Arif Rusyana *,a Yuskar Lase b

Department of Civil and Environmental Engineering, Universitas Indonesia, Depok, Indonesia

Article Info

Article History:

Received 29 Jan 2026

Accepted 01 July 2026

Keywords:

Data center building;
Base isolation;
Double concave friction pendulum;
Seismic performance-based design;
Seismic data center building design in developing countries

Abstract

Data centers are specialized facilities characterized by unique structural demands, typically featuring three times the seismic mass and twice the floor height of conventional buildings. To comply with the stringent annual downtime limits of Tier III and Tier IV classifications (1.6 and 0.4 hours, respectively), these facilities require operational continuity. This study evaluates their seismic performance in high-seismicity regions and examines the Telecommunications Industry Association (TIA-942) requirements regarding base isolation. A comparative nonlinear time history analysis (NLTHA) was conducted on a multi-story data center under Maximum Considered Earthquake (MCE_R) demands across three configurations: a baseline fixed-base structure (Risk Category II), a stiffened fixed-base structure (Risk Category IV), and a base-isolated system. The findings highlight a critical limitation in standard design approaches. Although the stiffened fixed-base model effectively resisted high inertial forces and limited drifts to code-compliant levels, it failed to mitigate peak floor accelerations. This potentially increases the risk of operational downtime, as peak floor accelerations in the server areas exceed the threshold. Within the scope of the analyzed models, the defined design parameters, and the established research limitations, this study demonstrates that conventionally stiffened fixed-base structures do not provide the acceleration control necessary for critical infrastructure. Therefore, base isolation proves to be an effective option to meet critical operational demands by controlling floor accelerations below the specified threshold. These findings support the TIA-942 standard provisions regarding the necessity of implementing base isolation to maintain the operational continuity.

1. Introduction

The enactment of the Republic of Indonesia's Law Number 27 of 2022 concerning Personal Data Protection (UU PDP) triggered a significant increase in the construction of data center facilities across the archipelago. However, Indonesia's geographical location within the Pacific Ring of Fire, a zone characterized by active tectonic plate movements, presents substantial seismic threats. These threats pose a risk of structural failure and physical damage, potentially causing operational outages or damage to IT assets, particularly the loss of digital data on motion-sensitive storage media, which ultimately compromises the fundamental performance objectives of the data center infrastructure. Critical digital data is typically housed in facilities rated as Tier III and Tier IV to ensure integrity and accessibility, even in the event of natural disasters, particularly earthquakes. The data center standards stipulate stringent maximum annual downtime limits: 1.6 hours for Tier III and 0.4 hours for Tier IV data centers [1]. This definition of downtime includes disruptions caused by natural disasters.

---

*Corresponding author: arif.rustana@ui.ac.id
a orcid.org/0009-0009-6388-9533; b orcid.org/0009-0008-8977-9423
DOI: http://dx.doi.org/10.17515/resm2026-1485st0129rs

Both ASCE 7 [2] and SNI 1726 [3] classify critical facilities required to remain operational after a disaster as Risk Category IV structures. These standards, however, only specify a design earthquake intensity level of 2/3 MCEr. The minimum performance target for structural components is the Immediate Occupancy level, while non-structural components must maintain an Operational status following a seismic event. In addition to requiring a Seismic Importance Factor (I_e) of 1.5 for linear analysis of structural and non-structural components, TIA 942B [4] explicitly specifies the application of passive protection systems, such as base isolation, under increased earthquake intensity levels (MCEr) for Tier IV. However, this specification often lacks a comprehensive rationale or quantitative justification. Consequently, in developing nations such as Indonesia, this provision is frequently overlooked or deemed non-mandatory.

2. Seismic Performance Requirements for Data Center Facilities

2.1 Vulnerability of Digital Data Storage Equipment

The fragility of Hard Disk Drives (HDDs) is one of the determining factors for data center vulnerability. Although robust flash-based NVMe drives are increasingly adopted, HDDs remain essential for long-term archival storage to prevent data degradation [5,6]. However, accelerations exceeding manufacturer tolerances can cause magnetic head damage and permanent data loss in HDDs. While Alhan and Gavin [7] and Erkus et al. [1] adopt a strict floor acceleration threshold of 0.2g based solely on common practice data from IT experts, Seagate, an HDD manufacturer [8], specifies a limit of 0.22g to protect this critical infrastructure.

2.2 Structural Characteristics and Seismic Mass

The seismic mass of data centers is significantly greater than that of conventional buildings. TIA 942B [4] specifies a minimum total load of 14.4 kPa (approximately three times the load of a typical office or residential building). Unlike standard structures, in which only approximately 25% of the live load contributes to the effective mass, ASCE 7 requires 100% inclusion of permanent equipment anchored to the structure, resulting in a much higher effective seismic weight.

2.3 Research Gap

While the effectiveness of base isolation is widely recognized [9–19], existing research has focused on conventional buildings designed for standard life-safety criteria. Studies specifically addressing data centers are very limited. For instance, Erkus et al. [1] explored base isolation for data centers using rubber bearings but limited their analysis to a single-story structure. This is a critical limitation because a single-story model cannot capture the vertical amplification of floor accelerations along the building's height. Alhan and Gavin [7] proposed a localized approach by isolating server racks. However, placing the isolation system at the base of the building offers a far more comprehensive benefit, as it improves the overall structural performance and effectively prevents the upward amplification of floor accelerations in multi-story buildings.

Other researchers have investigated multi-story structures using advanced sliding systems like FPS and DCFP (e.g., P. He et al. [11] and Imran et al. [14]). However, these models assume standard building masses, which are much lighter than the massive loads required in actual data centers. More importantly, these previous studies typically evaluate performance based on inter-story drift and total base shear, rather than checking if the actual floor accelerations exceed the specified acceleration thresholds. The choice of the isolation system presents another critical gap. Because elastomeric bearings are susceptible to physical degradation and struggle to safely provide the period elongation required to minimize floor accelerations [20,21], this study shifts the focus to DCFP. For heavy-mass data centers, DCFP offers the enhanced durability and kinematic stability to keep non-structural components fully operational [14]. This specific limitation in past research creates a critical knowledge gap, leaving the structural responses at upper stories unquantified. Furthermore, while the TIA 942B [4] standard recommends base isolation, it lacks the detailed quantitative justification to enforce it. Because of this, the recommendation is frequently overlooked or considered non-mandatory in developing nations like Indonesia. To directly address the shortcomings resulting from these previous single-story investigations, the novelty of this study lies in the focus on capturing the vertical amplification of floor accelerations in heavy-mass, multi-level structures—a critical design factor that is significantly underestimated in local engineering practices. Instead of adopting isolation technologies, local practitioners typically default to conventional fixed-base systems, attempting to satisfy the stringent demands of Risk Category IV facilities merely by increasing the structural capacity and member sizing.

2.4 Objectives

This study addresses the identified gaps by evaluating and comparing the structural response of all data center building models under MCEr ground motions, specifically focusing on structural element deformation limits, inter-story drift, and total base shear. Furthermore, it assesses the capability of each model to achieve Operational performance by limiting maximum floor accelerations below the 0.22g threshold.

3. Methodology

3.1 Research Flowchart

The comprehensive research methodology adopted in this study, spanning from the initial linear elastic design to the advanced nonlinear time history analysis and performance assessment, is schematically illustrated in Fig. 1.

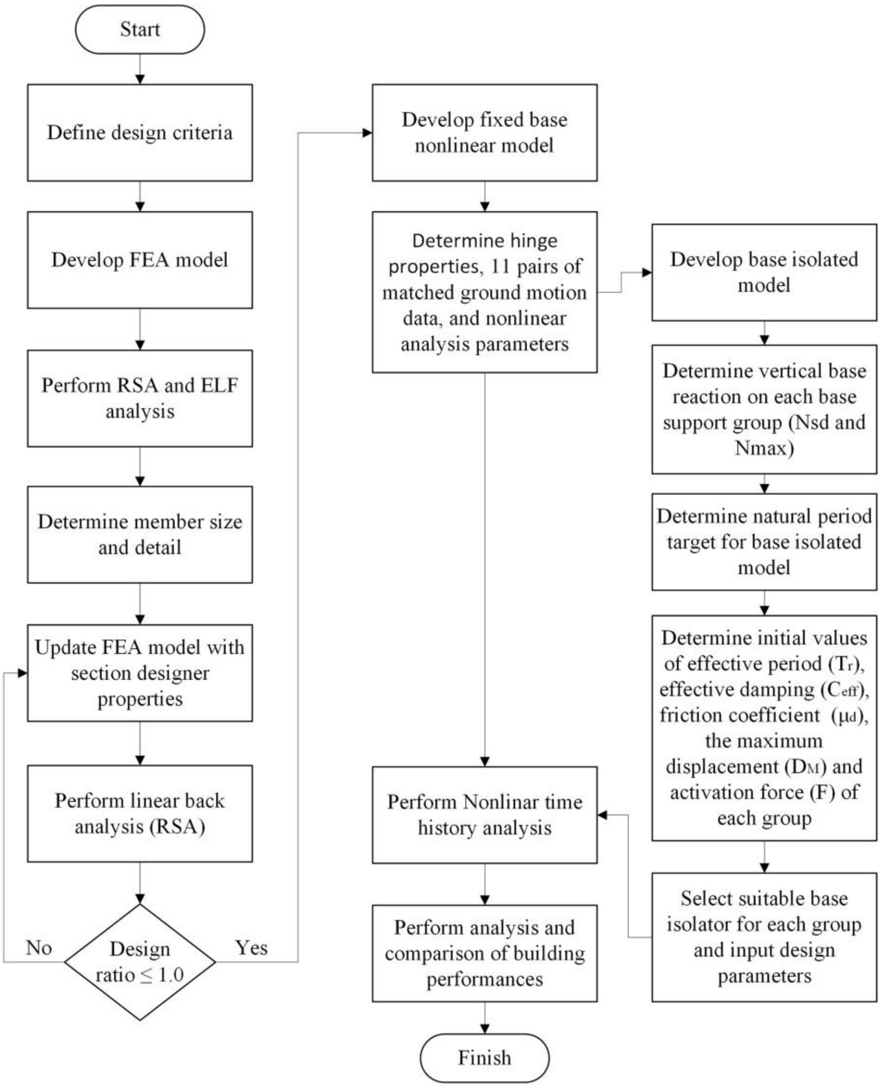

Fig. 1. Research methodology flowchart for the structural design and nonlinear performance evaluation. FEA = finite element analysis. RSA = response spectrum analysis. ELF = equivalent lateral force. N_{sd} = gravity combination axial support reaction. N_{max} = ultimate limit state combination axial support reaction.

3.2 Building Geometry and Configuration

A comparative analysis was conducted on a four-story data center modeled with both a conventional fixed-base system and a DCFP base isolation system, in compliance with ASCE 7 [2] and SNI 1726 [3]. The limitation to a four-story configuration is based on two primary structural considerations. First, this height restriction prevents uplift (tensile reactions) at the isolation interface, ensuring continuous contact between the slider and the concave surfaces of the DCFP bearings, in accordance with the recommended height-to-footprint aspect ratio limit of 2.0 [16]. Second, given the exceptionally large seismic mass inherent to data centers, this limitation is essential to satisfy the stringent floor acceleration thresholds across all levels housing the data racks. Furthermore, the structure is configured with a 6.0-meter floor-to-floor height to accommodate the substantial overhead Mechanical, Electrical, and Plumbing (MEP) utilities typical of such facilities. The structural layout utilizes a 10-meter column grid with six bays in each orthogonal direction, resulting in a total footprint of 60 m × 60 m.

3.3 Analysis Models

To evaluate seismic performance, three structural models were developed, as detailed in Table 1. Model 3 intentionally adopts the superstructure of Model 1 without additional strengthening to quantify the standalone effectiveness of the isolation system. Although combining base isolation with stiffer Risk Category IV detailing would technically provide better performance, retaining the standard Risk Category II baseline directly eliminates the need for the member upsizing typical of conventional fixed-base designs.

Table 1. Comparative characteristics and seismic design criteria of the three evaluated structural models

Parameter	Model 1	Model 2	Model 3
Description	Fixed-base baseline	Fixed-base strengthened	Base-isolated
Seismic Risk Category	II	IV	IV
Importance Factor (I_e)	1	1.5	N/A
Isolation System	None	None	DCFP (Isosism® PS)
Design Basis	SNI 1726, ASCE 7	SNI 1726, ASCE 7	SNI 1726, ASCE 7
Target Performance	Code minimum (Life Safety)	Operational	Operational

Note: Model 3 is directly analyzed using Nonlinear Time History Analysis (NLTHA). The superstructure adopts the configuration of Model 1 without additional strengthening (Risk Category II); therefore, the linear design Importance Factor is not defined or not applicable. DCFP = double concave friction pendulum.

3.4 Material Properties

The primary structural material is reinforced concrete with a specified compressive strength (f'_c) of 40 MPa for all structural components. For both flexural and shear demands, the reinforcement consists of ASTM A615 Grade 60 deformed bars, with a yield strength (f_y) of 420 MPa and an ultimate tensile strength (f_u) of 620 MPa. Detailed dimensions and reinforcement of each structural component are provided in Appendix 1.

3.5 Structural Analysis and Linear Design Parameters

The structure was modeled in CSI ETABS [22] as a dual system comprising intermediate RC moment frames and special RC shear walls. The linear design utilized the following seismic parameters: R = 6.5, Ω_0 = 2.5, and C_d = 5.

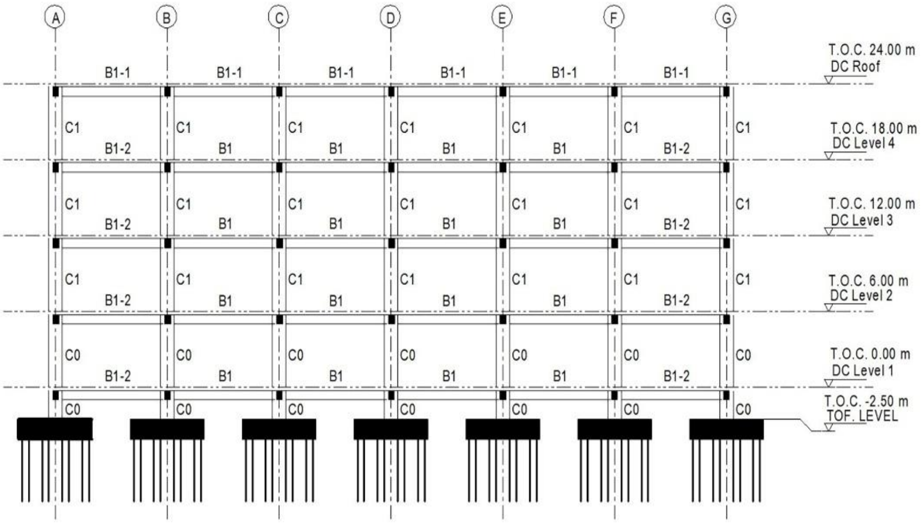

(a) Typical interior frame

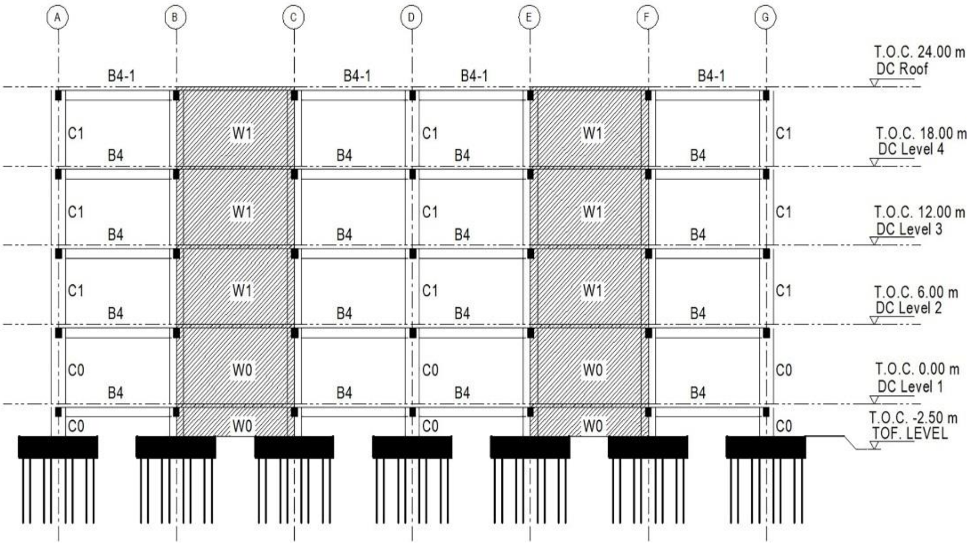

(b) Typical exterior frame

Fig. 2. Structural component details and elevation views for Model 1 and Model 2: (a) interior frame; (b) exterior frame

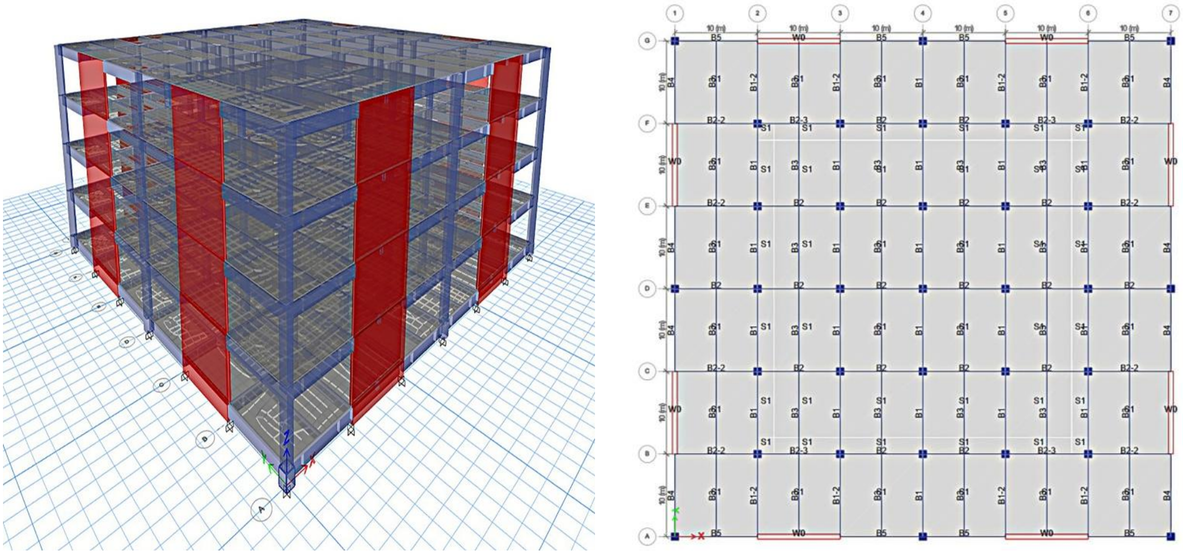

(a) 3D view

(b) Typical building layout

Fig. 3. Finite element structural models for Model 1 and Model 2: (a) three-dimensional view; (b) typical building floor layout

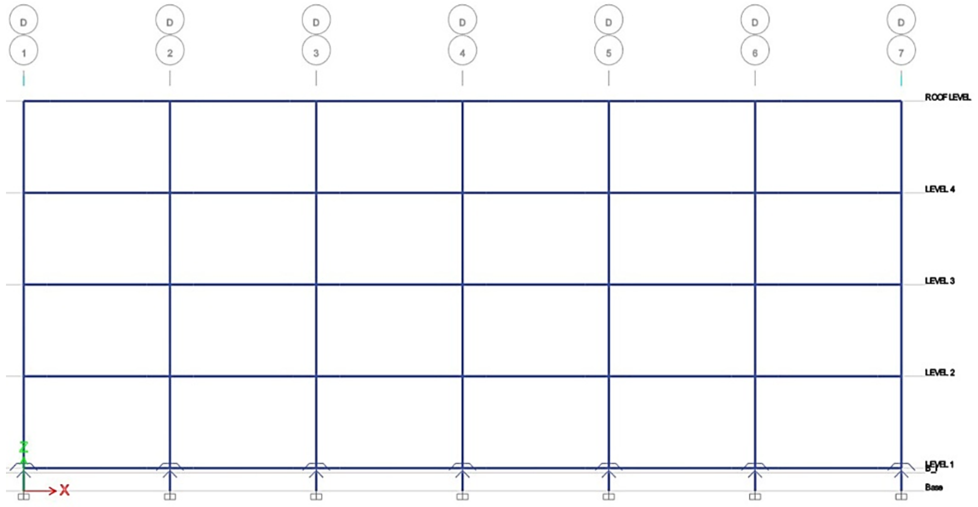

(a) Typical interior frame

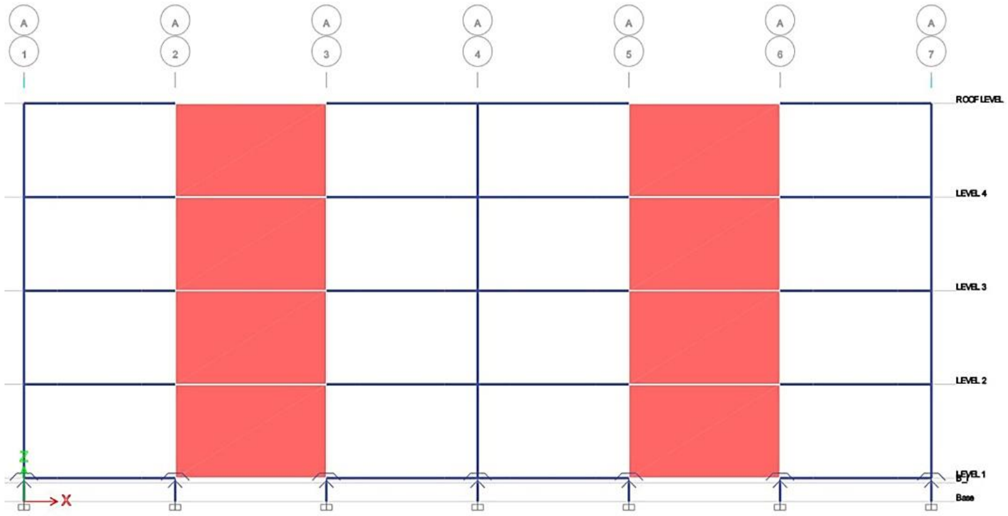

(b) Typical exterior frame

Fig. 4. Typical building elevation views of Model 3 (base-isolated structure): (a) interior frame; (b) exterior frame

3.6 Structural Loading Criteria

The structural loading criteria comply with the minimum requirements stipulated in TIA-942-B (2017) [4] and SNI 1727 (2020) [23]. The applied loads—comprising dead, live, seismic, and wind loads—are determined based on these standards. Since wind loads in tropical regions like Indonesia typically do not govern the design of mid-rise buildings, and considering the primary focus of this study on seismic resilience, wind effects are excluded from the analysis. Furthermore, Superimposed Dead Loads (SIDL) and Live Loads (LL) are assigned according to the specific functionality of each area; the detailed magnitudes for these loads are presented in Table 2.

Table 2. Superimposed dead loads and live loads for different functional areas

Legend	Rooms	Superimposed Dead Load (SIDL) (kPa)	Live Load (LL) (kPa)
🟦	Data Rack Hall	2.5	12+2.4
🟦	Access Corridor	2.5	12+2.4
🟥	Electrical & Instrument Area	2.5	10
🟩	Mechanical Area	5	16
⬜	General Area	2.5	5

Note: SIDL = superimposed dead load. LL = live load. The live load value "12+2.4" represents the sum of the floor live load and the load from hanging MEP (Mechanical, Electrical, and Plumbing) components.

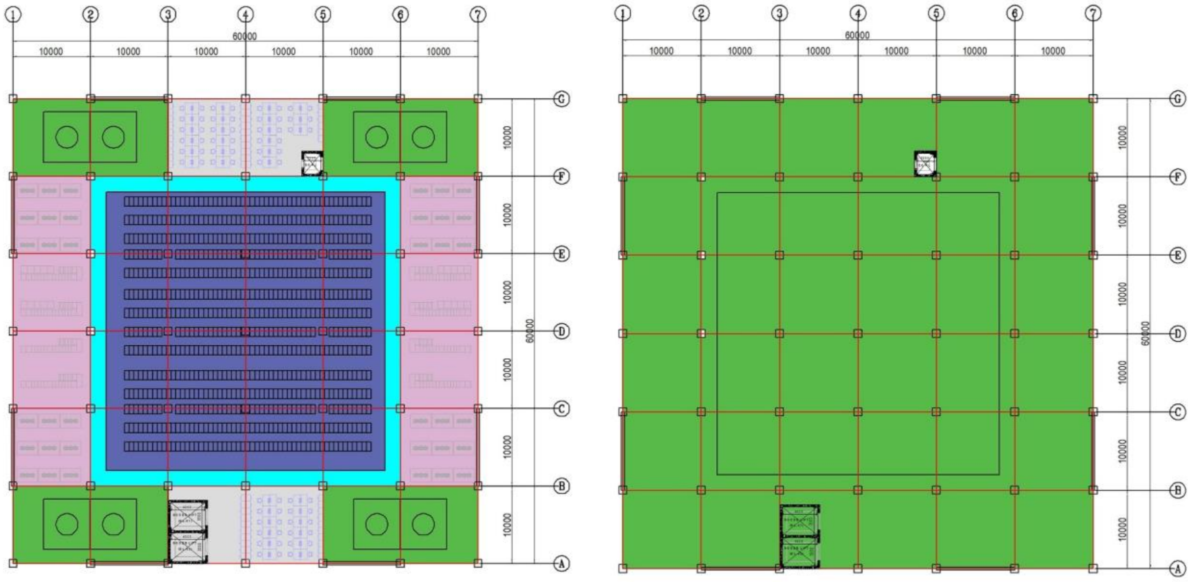

(a) Typical 1st to 4th floor loading map

(b) Roof level loading map

Fig. 5. Spatial distribution of design loads applied to the structural models: (a) typical 1st to 4th floor; (b) roof level

3.6.1 Seismic Loads

The seismic parameters utilized in this study were derived from the 2024 Indonesian Seismic Hazard Maps, published by PusGen [24], while ground motion time histories were selected based on the national Seismic Hazard Deaggregation Maps [3,25]. For the linear structural design, Response Spectrum Analysis (RSA) was employed and scaled against the Equivalent Lateral Force (ELF) method to satisfy the base shear requirements of SNI 1726 [3] and ASCE 7 [2]. This linear analysis applied the Jakarta-specific parameters detailed in Table 3, incorporating 100 vibration modes to achieve a cumulative mass participation ratio exceeding 98% in both principal directions.

Table 3. Linear seismic design parameters for Response Spectrum Analysis (RSA) in Jakarta

Parameter	Value
Site Class	SE
Mapped MCE$_G$ Peak Ground Acceleration (PGA)	0.408 g
MCE$_R$ spectral response acceleration, 5% damped, at short period 0.2 s (S_S)	0.867 g
MCE$_R$ spectral response acceleration, 5% damped, at 1 s period (S_1)	0.410 g
Short-period site coefficient at 0.2 s (F_a)	1.153
Long-period site coefficient at 1 s (F_v)	2.380
Design spectral response acceleration, 5% damped, at short period 0.2 s (S_{DS})	0.697 g
Design spectral response acceleration, 5% damped, at 1 s period (S_{D1})	0.650 g
Fundamental period parameter (T_0)	0.187 s
Short-period site parameter (T_S)	0.933 s
Long-period site parameter (T_L)	20 s

Note: MCE$_G$ = maximum considered earthquake geometric mean. MCE$_R$ = risk-targeted maximum considered earthquake. SE = soft soil profile.

3.6.2 Nonlinear Seismic Loads

Nonlinear Time History Analysis (NLTHA) using direct integration was employed to accurately assess structural performance. The selection of ground motions for South Jakarta followed the Indonesian Seismic Hazard Deaggregation Map [25] at the MCE$_R$ level (2,500-year return period). The controlling parameters (Mean Magnitude and Distance) and selected records are summarized in Table 4 and Table 5, respectively.

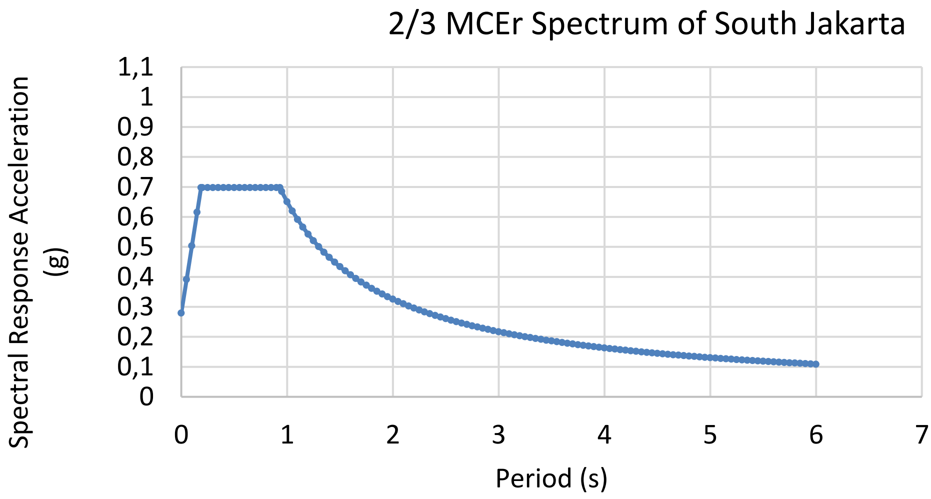

(a) Design Earthquake level (2/3 MCE$_R$)

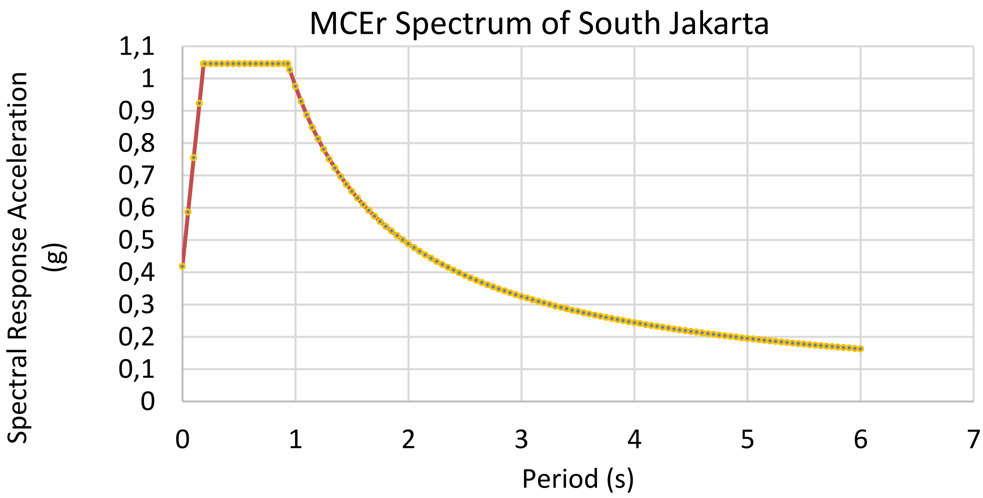

(b) Risk-Targeted Maximum Considered Earthquake level (MCE$_R$)

Fig. 6. Design response spectra for the South Jakarta region: (a) design earthquake level (2/3 MCE$_R$); (b) risk-targeted maximum considered earthquake level (MCE$_R$).

Table 4. Target parameters for the selection of ground motion data

Source	Magnitude (M_w)			Distance (km)		
	PGA	0.2 s	3.0 s	PGA	0.2 s	3.0 s
Benioff	7.2-7.4	7.2-7.4	7.4-7.6	120-150	120-150	120-150
Megathrust	8.6-8.8	8.6-8.8	8.6-8.8	150-200	150-200	150-200
Shallow Crustal	5.6-5.8	5.6-5.8	6.2-6.4	40-50	40-50	30-40

Note: PGA = peak ground acceleration. M_w = moment magnitude. Earthquake source parameters are determined based on the seismic deaggregation map of Indonesia (2022).

Table 5. List of eleven ground motion record pairs selected for the Jakarta region

Time History Data	Event Name	Year	Direction-1	Direction-2	M_w	Epicentral Distance (km)	Data Source, Station	Duration (s)
Megathrust	2844986	2010	EW	NS	8.81	227	Valdivia Hospital	79.00
	Tohoku	2011	EW	NS	9.12	279.75	41211	360.00
Benioff	Iwate off	2011	EW	NS	7.4	172.55	Kazuno	80.00
	Ki se	2004	EW	NS	7.41	154.06	Atsumi	229.70
Shallow Crustal	Northridge-02	1994	90	180	6.05	38.14	Anaverde Valley-City R	40.04
	Northwest China-02	1997	0	270	5.93	20.6	Jiashi	60.00
	Chi-Chi Taiwan-02	1999	N	E	5.9	46.91	Chy025	62.00

Time History Data	Event Name	Year	Direction-1	Direction-2	M_w	Epicentral Distance (km)	Data Source, Station	Duration (s)
	Northern Calif-01	1941	225	315	6.4	44.68	Ferndale City Hall	40.00
	Friuli Italy-02	1976	0	270	5.91	41.39	Codroipo	33.57
	Coyote Lake	1979	150	240	5.74	33.83	Halls Valley	60.00
	Victoria Mexico	1980	10	280	6.33	39.30	Sahop Casa Flores	15.74

Note: Mw = moment magnitude. N = North; E = East; EW = East-West; NS = North-South; Numerical values in the Direction columns represent the station's recording azimuth angles in degrees.

3.6.3 Ground Motion Modification (Spectral Matching)

In compliance with SNI 1726 [3] and ASCE 7 [2], time-domain spectral matching was performed directly in ETABS. This method scaled the records to the site-specific MCE_R target spectrum (Fig. 6), without altering their fundamental non-stationary characteristics or phase. The closely matched output spectra are illustrated in Fig. 7.

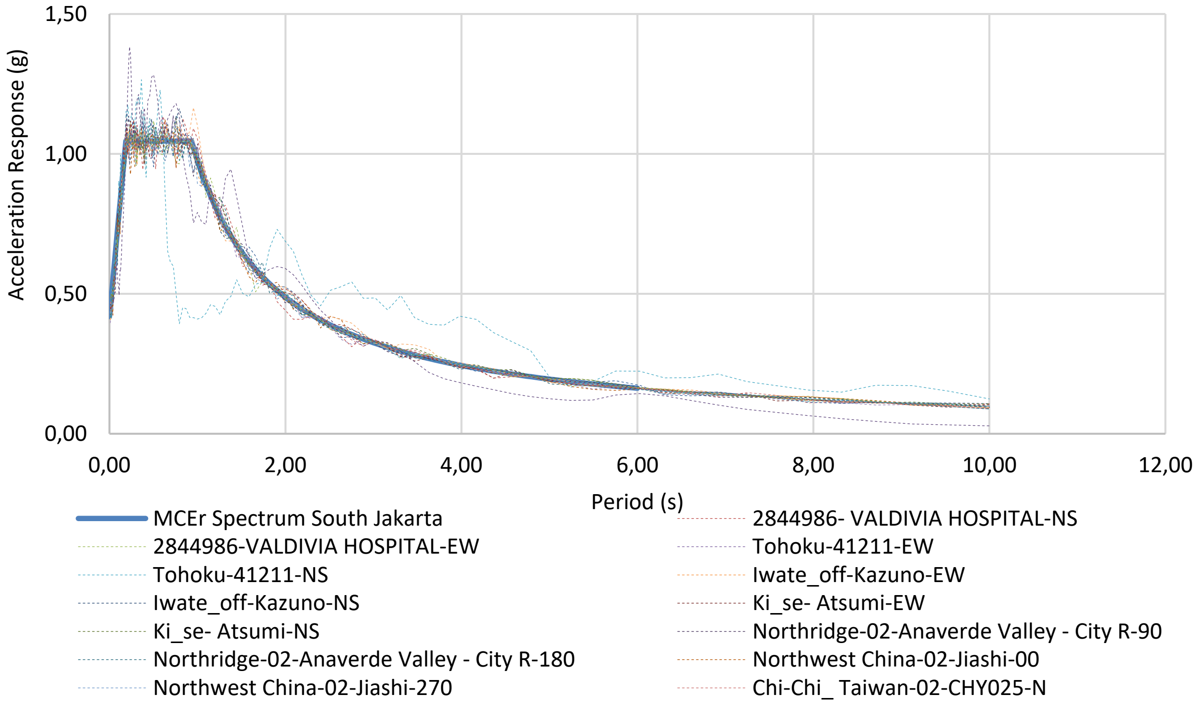

Fig. 7. Response spectra of the eleven ground motion record pairs spectrally matched to the South Jakarta Risk-Targeted Maximum Considered Earthquake (MCE_R) target spectrum

3.7 Nonlinear Analysis Algorithm and Material Modeling

NLTHA utilized the Hilber-Hughes-Taylor (HHT) direct integration method [26], with an alpha (α) parameter of -1/3 to mitigate spurious high-frequency modes. To ensure numerical stability and accuracy, the analysis was executed using a time step of 0.01 s, a stringent convergence tolerance of 10^{-4}, and a specified material damping ratio of 2.5% [2,3]. The material constitutive relationships adopted the Mander model [27] for confined concrete and a kinematic hardening model [28] for steel reinforcement, as illustrated in Fig. 8a and Fig. 8b, respectively.

3.8 Plastic Hinge Definition and Performance Criteria

The structural performance assessment adheres to specific deformation limits (Fig. 8c). Frame elements utilized lumped plastic hinges defined per Tables 10-7 (beams) and 10-8 (columns) of ASCE 41 [29], whereas shear walls employed fiber hinge modelling to accurately capture axial-flexural behavior based on section discretization. To ensure post-disaster operational status, the global performance objective strictly limits all component deformations to the Immediate Occupancy (IO) level [4].

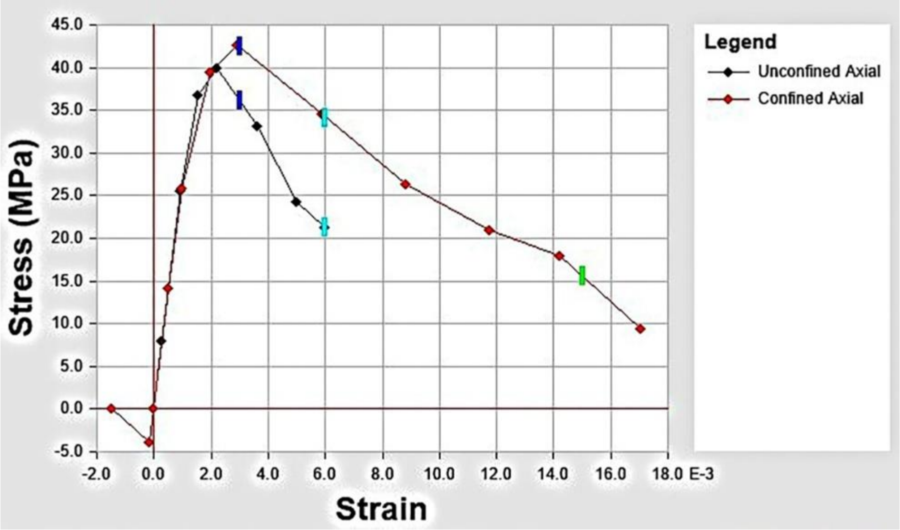

(a) Confined and unconfined concrete stress-strain model

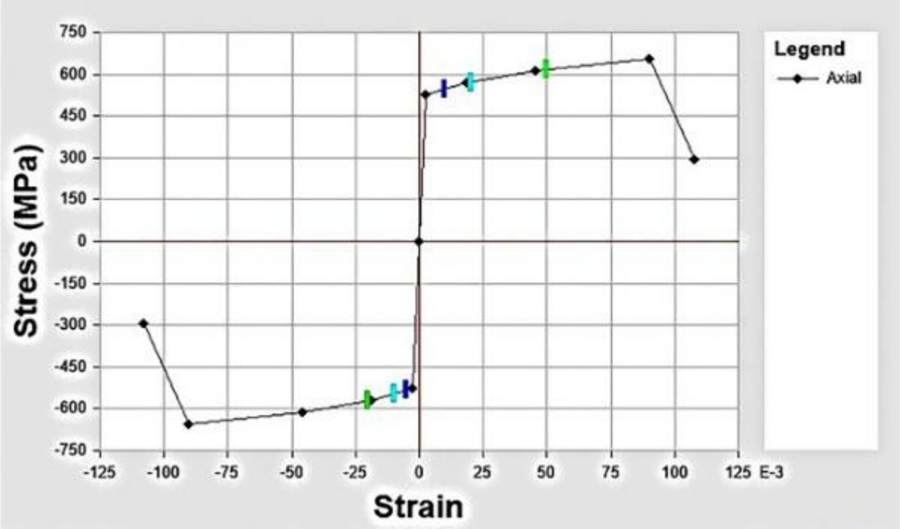

(b) Steel reinforcement stress-strain model

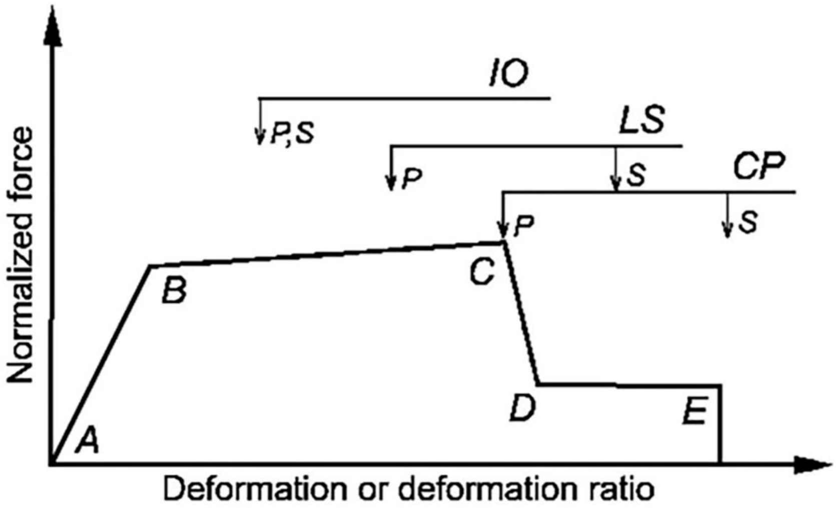

(c) Generalized backbone curve for structural performance assessment [29]

Fig. 8. Monotonic material stress-strain models and component performance criteria: (a) confined and unconfined concrete; (b) steel reinforcement; (c) generalized backbone curve for structural performance assessment

3.9 Base Isolation Design Procedure

The base-isolated structure (Model 3) was developed using the finalized superstructure design of the fixed-base model (Model 1), retaining identical cross-sectional dimensions and reinforcement detailing. The design and selection of the estimated isolation devices were conducted in accordance with the technical guidelines provided by Freyssinet for the Isosism® PS Pendulum System [30].

3.9.1 Device Selection

The selection process commenced with the identification of vertical reaction forces at each column support. Based on the magnitude of these reactions under gravity loads, the isolators were categorized into four distinct groups (Table 6). The coefficient of friction for each group, as shown in Table 7, was determined using the friction-vertical load relationship curve. This value depends on the contact pressure derived from the ratio of gravity loads to the maximum reaction forces under seismic load combinations.

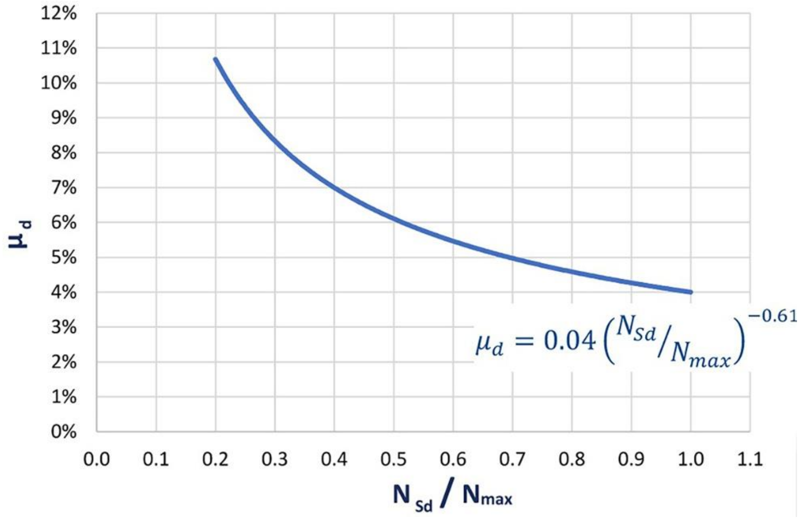

Fig. 9. Dependency of the dynamic friction coefficient (μ_d) on the normalized vertical load ratio ($N_{\mathrm{Sd}}/N_{\max}$) for the ISOSISM® PS isolator [30] with unlubricated ISOGLIDE®. N_{Sd} = gravity combination axial support reaction. $N_{\max}$ = ultimate limit state combination axial support reaction

Concerning the frictional characteristics of the sliding interface, the manufacturer's technical specifications for the ISOGLIDE® material provide critical distinctions regarding the dynamic friction coefficient. While the friction coefficient is theoretically influenced by both sliding velocity and contact pressure, the specifications indicate that the velocity dependence is negligible within the velocity range typical of seismic excitation for isolated structures. This explains the manufacturer's recommendation to assign identical values to both the fast and slow friction coefficients, resulting in a rate parameter that effectively approaches zero. Conversely, pressure dependence is significant and cannot be disregarded; specifically, the friction coefficient exhibits a non-linear inverse relationship with the vertical load, decreasing as the contact pressure increases [30].

Table 6. Column reaction and dynamic friction coefficients

Group	Column Position	N_{sd} (kN)	$N_{\max}$ (kN)	μ
A	Corner Columns	4075	5613	0.049
B	Perimeter Columns	6758	9543	0.049
C	Interior Columns	13722	19592	0.050
D	Shear walls	8177	11364	0.049

Note: DL = dead load. LL = live load. ULS = ultimate limit state. N_{Sd} = seismic design axial reaction. $N_{\max}$ = ultimate limit state combination axial support reaction. μ = dynamic friction coefficient.

3.9.2 Target Period and Radius of Curvature

Motion across two concave interfaces initiates once the horizontal seismic demand exceeds the static friction threshold, with the subsequent force-displacement behavior governed by horizontal and vertical force equilibrium. As expressed in Equation 1, the lateral recovery mechanism of the DCFP system consists of the sliding friction force (F_f) and the gravity-induced restoring force (F_R). These forces are generated during a lateral displacement (d) along a concave surface with an equivalent radius (R_{eq}), as illustrated by the mechanical model and free-body diagram of the DCFP in Fig. 10.

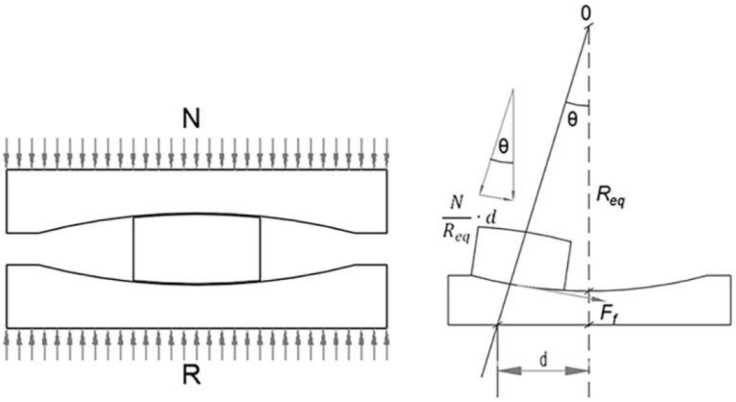

Fig. 10. Mechanical model and free-body diagram of the double concave friction pendulum (DCFP) system

$$F = F_f + F_R = \mu_d \cdot N + \frac{N}{R_{eq}} \cdot d \tag{1}$$

A primary performance objective for the data center is to limit the maximum floor acceleration to 0.22g [8]. Referring to the $\mathrm{MCE_R}$ design spectrum for South Jakarta (Fig. 6), a spectral acceleration of 0.22g corresponds to a structural period of 4.9 seconds. Consequently, this value $T_{\mathrm{D}} = 4.9$ s was adopted as the target effective period for the isolation system. According to the pendulum principle, the period of the system is governed primarily by the radius of curvature R_{eq} of the sliding surface, as expressed in Equation 2:

$$T_D = 2\pi \sqrt{\frac{R_{eq}}{g}} \tag{2}$$

where T_{D} is the vibration period of the isolation system, R_{eq} is the radius of curvature of the concave surface, and g is the gravitational acceleration. Solving for R_{eq} gives a required radius of 5.725 m. Based on available manufacturing specifications for the ISOSISM® pendulum [30], a standard device with a radius of curvature R_{eq} = 6 m was selected, as it closely approximates the calculated requirement. The effective damping of the DCFP device, as presented in Equation 3.

$$\xi_{eff} = \frac{2\mu_d}{\pi\left(\mu_d + \frac{d}{R_{eq}}\right)} \tag{3}$$

3.9.3 Iterative Design Process

To finalize the specific device properties for each group in Table 7, an iterative design procedure was employed. Initial parameters included a maximum displacement ($d = D_{\mathrm{M}}$), an initial damping ratio of 5%, and a target system acceleration of 0.22g. The derivation begins with the fundamental undamped equation of motion, where mass (m) and stiffness (k) relate to acceleration ($\ddot{u}$). Equation 4 demonstrates the relationship between acceleration and deformation in the base isolation system, illustrating that maximum displacement coincides with maximum acceleration and zero velocity, establishing a correlation between acceleration and the squared circular frequency (ω^2), where $\omega^2 = \frac{k}{m} = \left(\frac{2\pi}{T_{\mathrm{D}}}\right)^2$. By substituting the spectral acceleration ($\ddot{u} = S_{\mathrm{a}} \cdot g$) into Equation 4 and utilizing the effective period T_D defined in Equation 2, the relationship between the maximum displacement (D_M), the spectral acceleration ($S_{a(\xi)}$), and the equivalent radius of curvature of the DCFP (R_{eq}) is derived, as expressed in Equation 5.

$$m\ddot{u} = k \cdot D_M;\ \ddot{u} = \omega^2 D_M \tag{4}$$

$$D_M = S_{a(\xi)} \cdot R_{eq} \tag{5}$$

The initial stiffness (K_i) was assumed to be 100 times the effective stiffness (K_{eff}). Physically, this assumption accounts for the pre-sliding condition where the slider is tightly wedged between two sliding surfaces, resulting in a very high stiffness before the activation force is exceeded. Adopting these values serves as a robust numerical approach to comprehensively model this initial stiffness, a definition that aligns with the approach used in previous studies, such as by Imran et al. [14]. The iteration updates the design displacement for the next step ($t + 1$) based on the current step (t) using the spectral acceleration relationship adjusted for damping:

$$S_{a(\xi)} = S_{a(5\%)}\sqrt{\frac{5\%}{\xi}} \tag{6}$$

where $S_{a(\xi)}$, as presented in Equation 6, is the spectral acceleration at the system's effective damping ratio ξ, and $S_{a(5\%)}$ is the spectral acceleration at 5% damping. The iterative process continues until convergence is achieved, defined as a difference of less than 1% between the displacement values of consecutive steps, $D_{M(t+1)}$ and $D_{M(t)}$. The vertical stiffness (K_v) of each DCFP device was modeled based on the physical dimensions of its internal slider as expressed in Equation 8, while the required slider diameter (d_s), defined in Equation 7, was determined by the maximum ultimate limit state (ULS) axial reaction (N_{max}) and the sliding material's bearing capacity (ϕf_y = 135 MPa), where ϕ = 0.75 and f_y = 180 MPa [31]. E, A, and H represent the slider's elastic modulus, cross-sectional area, and effective height, respectively.

$$d_s = \sqrt{\frac{4N_{max}}{\pi \phi f_y}} \tag{7}$$

$$K_v = \frac{E \cdot A}{H} \tag{8}$$

Table 7. Linear and nonlinear parameters of the base isolation system for each isolator group

	Horizontal Base Isolation Parameters							Vertical Base Isolation Parameters			
	Linear Parameter		Non-Linear Parameter								
Group	K_{eff} (kN/m)	C_{eff} (kN-s/m)	K_i (kN/m)	μ_{fast}	μ_{slow}	Rate parameter	R_{eq} (m)	d_s (m)	A (m^2)	K_v (kN/m)	C_v (kN-s/m)
A	1475.87	1224.6	147586.8	0.049	0.049	0.0	6.0	0.25	0.045	90320788	28480.9
B	2503.24	2079.4	250323.5	0.049	0.049	0.0	6.0	0.35	0.089	177028746	51989.6
C	5213.66	4431.8	521365.9	0.050	0.05	0.0	6.0	0.45	0.146	292639355	95779.2
D	3002.98	2560.8	300298.1	0.049	0.049	0.0	6.0	0.35	0.089	177028746	56733.4

Note: K_{eff} = effective stiffness. C_{eff} = effective damping. K_i = initial stiffness. μ_{fast} = fast friction coefficient. μ_{slow} = slow friction coefficient. R_{eq} = equivalent net pendulum radius. d_s = slider diameter. A = slider section area. K_v = vertical stiffness. C_v = vertical damping.

3.10 Comparative Evaluation Criteria

The NLTHA evaluated three configurations: Model 1 (Fixed-base, Risk Category II), Model 2 (Fixed-base, Risk Category IV), and Model 3 (Base-isolated). To address TIA-942B [4] operational requirements, the discussion focuses on the governing maximum response from the two orthogonal directions.

3.10.1 Structural Performance Parameters

To verify structural performance, the evaluation focused on: (1) inelastic deformation mechanisms to map plastic hinge distributions; (2) total base shear to quantify seismic demand reduction; and (3) inter-story drift to assess lateral deformation compatibility.

3.10.2 Non-Structural Performance Parameters

The operational status of the non-structural performance is assessed based on floor acceleration limits. Although TIA-942B [4] emphasizes continuity without explicit quantitative thresholds, this study adopts a 0.22g floor acceleration limit [8], which represents a floor-level demand indicator for server areas under MCE_R events. Meeting this critical threshold aims to mitigate the risk of physical damage to sensitive data storage media, thereby supporting uninterrupted service.

4. Results and Discussion: Comparative Performance Analysis

This section presents the results of a comprehensive performance analysis and comparison across the structural models considered. Although the building has a symmetrical floor plan configuration, the ground motion amplitudes differ between the two orthogonal directions. The structural response is examined at the maximum values of the two principal directions reported and analyzed to ensure a robust comparative study.

4.1 Structural Performance Based on Plastic Hinge Formation

Structural performance is evaluated based on the inelastic deformation limits of the plastic hinges formed in the primary components. To facilitate the analysis, the results are categorized by component type: (1) beams, (2) columns, and (3) shear walls.

4.1.1 Beam Hinge Formation

Fig. 11 and Table 8 compare the plastic hinge distribution of the beams, across a total of 760 beam joints. Model 1 shows significant hinge formation in the critical Life Safety-Collapse Prevention (LS-CP) range. Model 2 reduces this damage but still shows widespread yielding. In contrast, Model 3 remains largely in the linear elastic (A-B) range, with only an average of 3% of hinges forming at the Immediate Occupancy (B-IO) level.

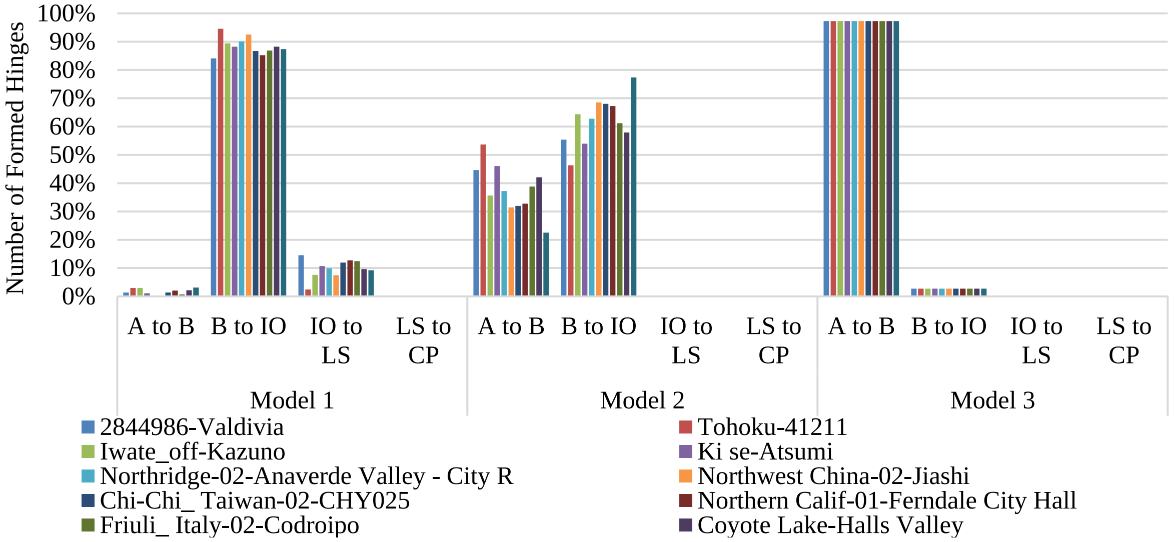

Fig. 11. Percentage of plastic hinges formed in beams across various ASCE 41 performance levels under MCE_R ground motions for Model 1 (standard fixed-base baseline for Risk Category II), Model 2 (stiffened fixed-base for Risk Category IV), and Model 3 (base-isolated utilizing the Model 1 superstructure). The hinge performance corresponds to the ASCE 41 generalized backbone curve previously illustrated in Fig. 8c, where A-B represents the linear elastic range, IO = Immediate Occupancy, LS = Life Safety, and CP = Collapse Prevention

Table 8. Summary of beam hinge formation percentages

		Time History													
Model	Range	1	2	3	4	5	6	7	8	9	10	11	$\bar{x}$	s	$x_{\max}$
1	A to B	1%	3%	3%	1%	0%	0%	1%	2%	1%	2%	3%	2%	1%	3%
	B to IO	84%	95%	89%	88%	90%	93%	87%	85%	87%	88%	87%	88%	3%	95%
	IO to LS	15%	2%	8%	11%	10%	7%	12%	13%	12%	10%	9%	10%	3%	15%
	LS to CP	0%	0%	0%	0%	0%	0%	0%	0%	0%	0%	0%	0%	0%	0%
2	A to B	45%	54%	36%	46%	37%	31%	32%	33%	39%	42%	23%	38%	9%	54%
	B to IO	55%	46%	64%	54%	63%	69%	68%	67%	61%	58%	77%	62%	8%	77%
	IO to LS	0%	0%	0%	0%	0%	0%	0%	0%	0%	0%	0%	0%	0%	0%
	LS to CP	0%	0%	0%	0%	0%	0%	0%	0%	0%	0%	0%	0%	0%	0%
3	A to B	97%	97%	97%	97%	97%	97%	97%	97%	97%	97%	97%	97%	0%	97%
	B to IO	3%	3%	3%	3%	3%	3%	3%	3%	3%	3%	3%	3%	0%	3%
	IO to LS	0%	0%	0%	0%	0%	0%	0%	0%	0%	0%	0%	0%	0%	0%
	LS to CP	0%	0%	0%	0%	0%	0%	0%	0%	0%	0%	0%	0%	0%	0%

Note: Model 1 = standard fixed-base baseline (Risk Category II); Model 2 = stiffened fixed-base (Risk Category IV); Model 3 = base-isolated (utilizing the Model 1 superstructure). All time history analyses were evaluated at the Maximum Considered Earthquake (MCE_R) demand level. Time History representations: 1 = 2844986-Valdivia; 2 = Tohoku-41211; 3 = Iwate-off-Kazuno; 4 = Kii se-Atsumi; 5 = Northridge-02-Anaverde Valley - City R; 6 = Northwest China-02-Jiashi; 7 = Chi Chi-Taiwan-02-CHY025; 8 = Northern Calif-01-Ferndale City Hall; 9 = Friuli-Italy-02-Codroipo; 10 = Coyote Lake-Halls Valley; 11 = Victoria Mexico-Sahop Casa Flores. IO = Immediate Occupancy; LS = Life Safety; CP = Collapse Prevention. $\bar{x}$ = mean; s = standard deviation; $x_{\max}$ = maximum value.

4.1.2 Column Hinge Formation

Fig. 12 and Table 9 compare the plastic hinge distribution in columns across 264 column joints, indicating that no hinges formed in the critical IO-CP range for any model. However, a slight plastic deformation (B-IO range) is observed in Model 1, whereas the columns in Model 2 and Model 3 remain completely elastic (A-B range).

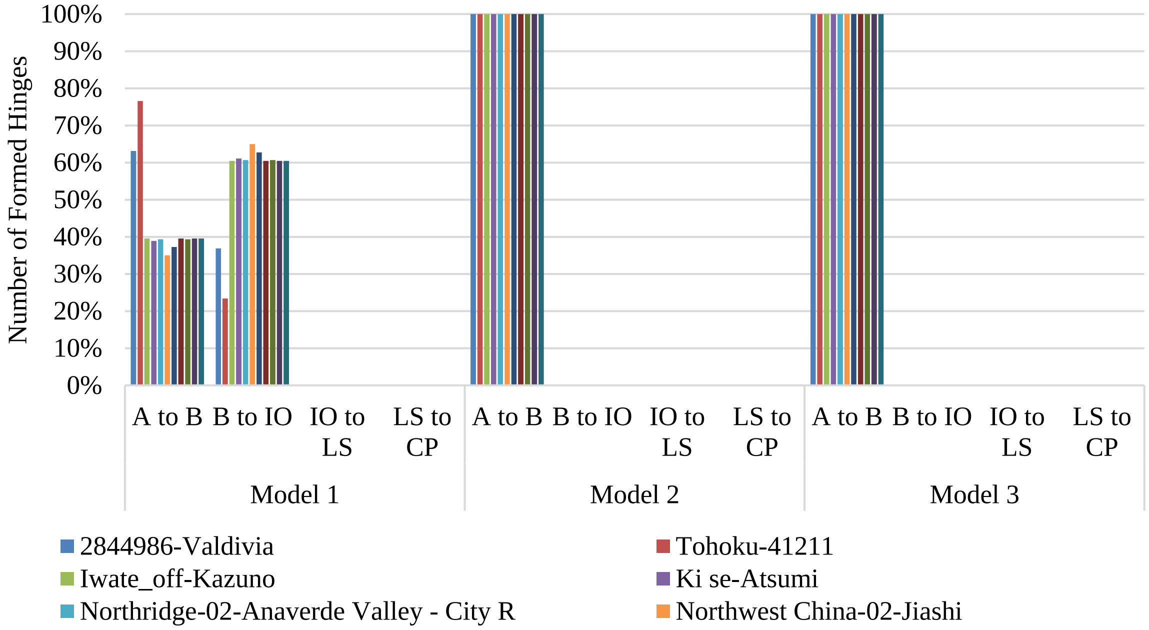

Fig. 12. Percentage of plastic hinges formed in columns across various ASCE 41 performance levels under MCE_R ground motions for Model 1 (standard fixed-base baseline for Risk Category II), Model 2 (stiffened fixed-base for Risk Category IV), and Model 3 (base-isolated utilizing the Model 1 superstructure). The hinge performance corresponds to the ASCE 41 generalized backbone curve previously illustrated in Fig. 8c, where A-B represents the linear elastic range, IO = Immediate Occupancy, LS = Life Safety, and CP = Collapse Prevention.

Table 9. Summary of column hinge formation percentages

Model	Range	Time History 1	2	3	4	5	6	7	8	9	10	11	$\bar{x}$	s	x_{max}
1	A to B	63%	77%	40%	39%	39%	35%	37%	40%	39%	40%	40%	44%	13%	77%
	B to IO	37%	23%	60%	61%	61%	65%	63%	60%	61%	60%	60%	56%	13%	65%
	IO to LS	0%	0%	0%	0%	0%	0%	0%	0%	0%	0%	0%	0%	0%	0%
	LS to CP	0%	0%	0%	0%	0%	0%	0%	0%	0%	0%	0%	0%	0%	0%
2	A to B	100%	100%	100%	100%	100%	100%	100%	100%	100%	100%	100%	100%	0%	100%
	B to IO	0%	0%	0%	0%	0%	0%	0%	0%	0%	0%	0%	0%	0%	0%
	IO to LS	0%	0%	0%	0%	0%	0%	0%	0%	0%	0%	0%	0%	0%	0%
	LS to CP	0%	0%	0%	0%	0%	0%	0%	0%	0%	0%	0%	0%	0%	0%
3	A to B	100%	100%	100%	100%	100%	100%	100%	100%	100%	100%	100%	100%	0%	100%
	B to IO	0%	0%	0%	0%	0%	0%	0%	0%	0%	0%	0%	0%	0%	0%
	IO to LS	0%	0%	0%	0%	0%	0%	0%	0%	0%	0%	0%	0%	0%	0%
	LS to CP	0%	0%	0%	0%	0%	0%	0%	0%	0%	0%	0%	0%	0%	0%

Note: Model 1 = standard fixed-base baseline (Risk Category II); Model 2 = stiffened fixed-base (Risk Category IV); Model 3 = base-isolated (utilizing the Model 1 superstructure). All time history analyses were evaluated at the Maximum Considered Earthquake (MCE_R) demand level. Time History representations: 1 = 2844986-Valdivia; 2 = Tohoku-41211; 3 = Iwate-off-Kazuno; 4 = Kii se-Atsumi; 5 = Northridge-02-Anaverde Valley - City R; 6 = Northwest China-02-Jiashi; 7 = Chi Chi-Taiwan-02-CHY025; 8 = Northern Calif-01-Ferndale City Hall; 9 = Friuli-Italy-02-Codroipo; 10 = Coyote Lake-Halls Valley; 11 = Victoria Mexico-Sahop Casa Flores. IO = Immediate Occupancy; LS = Life Safety; CP = Collapse Prevention. $\bar{x}$ *= mean; s = standard deviation;* x_{max} *= maximum value.*

4.1.3 Shear Wall Hinge Formation

Fig. 13 and Table 10 compare the plastic hinge formation in shear walls across 40 monitored hinge locations. Model 1 shows degradation in the LS-CP range. Model 3 shows the highest performance, effectively limiting the response to the linear elastic (A-B) range.

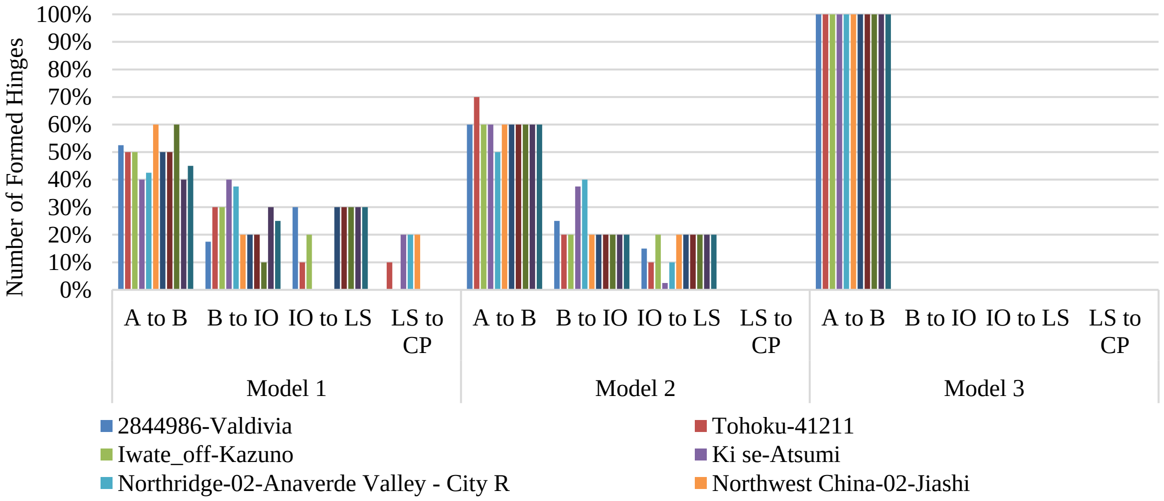

Fig. 13. Percentage of plastic hinges formed in shear wall across various ASCE 41 performance levels under MCE_R ground motions for Model 1 (standard fixed-base baseline for Risk Category II), Model 2 (stiffened fixed-base for Risk Category IV), and Model 3 (base-isolated utilizing the Model 1 superstructure). The hinge performance corresponds to the ASCE 41 generalized backbone curve previously illustrated in Fig. 8c, where A-B represents the linear elastic range, IO = Immediate Occupancy, LS = Life Safety, and CP = Collapse Prevention.

Table 10. Summary of shear wall hinge formation percentages

		Time History													
Model	Range	1	2	3	4	5	6	7	8	9	10	11	$\bar{x}$	s	$x_{\max}$
1	A to B	53%	50%	50%	40%	43%	60%	50%	50%	60%	40%	45%	49%	7%	60%
	B to IO	18%	30%	30%	40%	38%	20%	20%	20%	10%	30%	25%	25%	9%	40%
	IO to LS	30%	10%	20%	0%	0%	0%	30%	30%	30%	30%	30%	19%	14%	30%
	LS to CP	0%	10%	0%	20%	20%	20%	0%	0%	0%	0%	0%	6%	9%	20%
2	A to B	60%	70%	60%	60%	50%	60%	60%	60%	60%	60%	60%	60%	4%	70%
	B to IO	25%	20%	20%	38%	40%	20%	20%	20%	20%	20%	20%	24%	8%	40%
	IO to LS	15%	10%	20%	3%	10%	20%	20%	20%	20%	20%	20%	16%	6%	20%
	LS to CP	0%	0%	0%	0%	0%	0%	0%	0%	0%	0%	0%	0%	0%	0%
3	A to B	100%	100%	100%	100%	100%	100%	100%	100%	100%	100%	100%	100%	0%	100%
	B to IO	0%	0%	0%	0%	0%	0%	0%	0%	0%	0%	0%	0%	0%	0%
	IO to LS	0%	0%	0%	0%	0%	0%	0%	0%	0%	0%	0%	0%	0%	0%
	LS to CP	0%	0%	0%	0%	0%	0%	0%	0%	0%	0%	0%	0%	0%	0%

Note: Model 1 = standard fixed-base baseline (Risk Category II); Model 2 = stiffened fixed-base (Risk Category IV); Model 3 = base-isolated (utilizing the Model 1 superstructure). All time history analyses were evaluated at the Maximum Considered Earthquake (MCE_R) demand level. Time History representations: 1 = 2844986-Valdivia; 2 = Tohoku-41211; 3 = Iwate-off-Kazuno; 4 = Kii se-Atsumi; 5 = Northridge-02-Anaverde Valley - City R; 6 = Northwest China-02-Jiashi; 7 = Chi Chi-Taiwan-02-CHY025; 8 = Northern Calif-01-Ferndale City Hall; 9 = Friuli-Italy-02-Codroipo; 10 = Coyote Lake-Halls Valley; 11 = Victoria Mexico-Sahop Casa Flores. IO = Immediate Occupancy; LS = Life Safety; CP = Collapse Prevention. $\bar{x}$ = mean; s = standard deviation; $x_{\max}$ = maximum value.

4.2 Comparison of Total Base Shear Responses

Fig. 14 and Table 11 present the maximum total base shear record for each model. The fixed-base Model 2 recorded a mean base shear 6% higher than Model 1. Conversely, the base-isolated Model 3 resulted in a mean base shear approximately 67% lower than the fixed-base baselines.

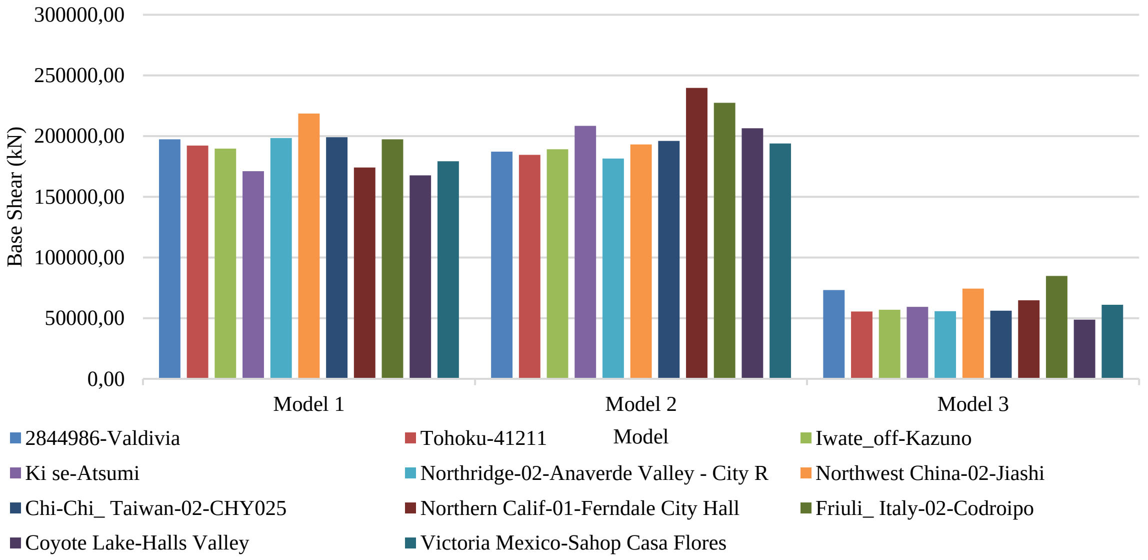

Fig. 14. Comparison of total base shear demands for Model 1 (standard fixed-base baseline for Risk Category II), Model 2 (stiffened fixed-base for Risk Category IV), and Model 3 (base-isolated utilizing the Model 1 superstructure) under MCE_R-level ground motions.

Table 11. Summary of total base shear responses (kN)

Time History	Model 1	Model 2	Model 3
1	197392.81	187147.95	73232.67
2	192156.32	184524.97	55475.32
3	189767.50	189229.08	56912.31
4	171075.81	208421.20	59292.47
5	198373.65	181475.61	55777.23
6	218639.29	193177.69	74396.86
7	199122.62	196062.56	56135.72

Time History	Model 1	Model 2	Model 3
8	174084.84	239794.13	64686.96
9	197306.75	227447.19	84821.48
10	167630.38	206440.91	48707.57
11	179341.93	193960.53	60991.38
$\bar{x}$	189535.63	200698.35	62766.36
$x_{\max}$	218639.29	239794.13	84821.48
s	15196.50	18456.16	10620.92

Note: Model 1 = standard fixed-base baseline (Risk Category II); Model 2 = stiffened fixed-base (Risk Category IV); Model 3 = base-isolated (utilizing the Model 1 superstructure). All time history analyses were evaluated at the Maximum Considered Earthquake (MCE$_R$) demand level. Time History representations: 1 = 2844986-Valdivia; 2 = Tohoku-41211; 3 = Iwate-off-Kazuno; 4 = Ki se-Atsumi; 5 = Northridge-02-Anaverde Valley - City R; 6 = Northwest China-02-Jiashi; 7 = Chi Chi-Taiwan-02-CHY025; 8 = Northern Calif-01-Ferndale City Hall; 9 = Friuli-Italy-02-Codroipo; 10 = Coyote Lake-Halls Valley; 11 = Victoria Mexico-Sahop Casa Flores. $\bar{x}$ = mean; s = standard deviation; $x_{\max}$ = maximum value.

4.3 Inter-Story Drift Response

Fig. 15 and Table 12 compare inter-story drift profiles against the 1.0% limit for Risk Category IV structures (ASCE 7; SNI 1726) under MCE$_R$ ground motions. Whereas Model 1 exceeded the limit, Model 2 successfully maintained drift levels below this threshold. Model 3 experienced an average inter-story drift of only 0.2%, displaying a uniform profile characteristic of rigid body motion.

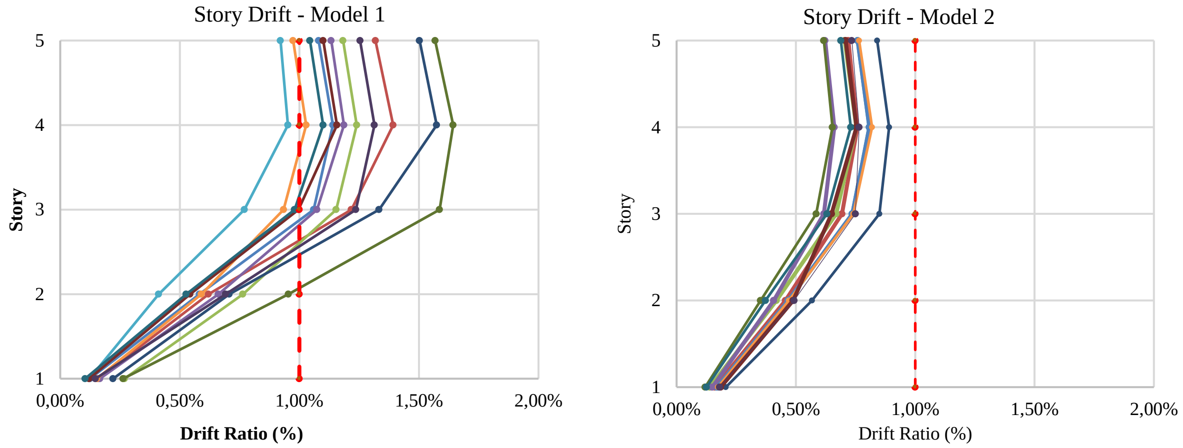

(a) Model 1

(b)Model 2

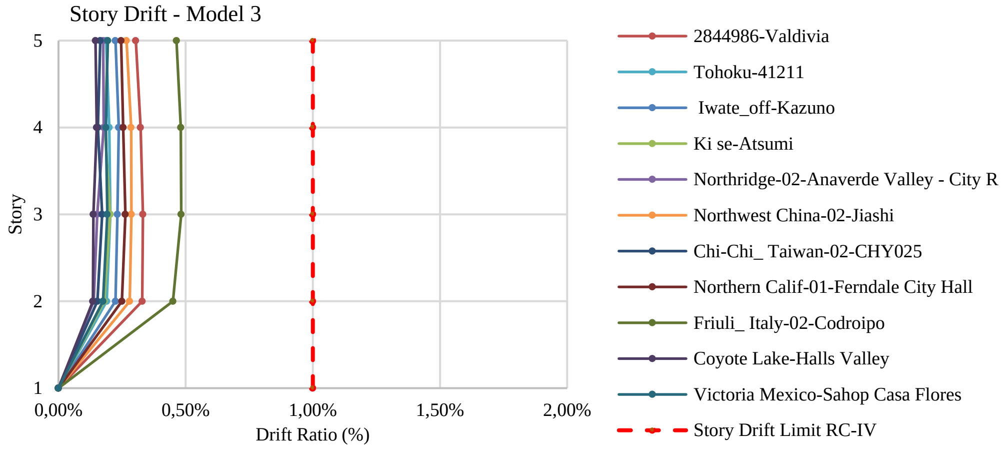

(c) Model 3

Fig. 15. Inter-story drift responses under MCE$_R$ ground motions: (a) Model 1 (standard fixed-base baseline for Risk Category II); (b) Model 2 (stiffened fixed-base for Risk Category IV); (c) Model 3 (base-isolated utilizing the Model 1 superstructure). The red dashed line denotes the 1.0% story drift limit specified in the TIA-942B standard for Risk Category IV (RC-IV) structures under MCE$_R$ ground motions.

Table 12. Summary of story drift response (%)

		Time History													
Model	Story	1	2	3	4	5	6	7	8	9	10	11	$\bar{x}$	s	$x_{\max}$
1	1	0.2%	0.1%	0.1%	0.3%	0.2%	0.2%	0.2%	0.1%	0.3%	0.2%	0.1%	0.2%	0.06%	0.3%
	2	0.6%	0.4%	0.6%	0.8%	0.7%	0.6%	0.7%	0.5%	1.0%	0.7%	0.5%	0.6%	0.14%	1.0%
	3	1.2%	0.8%	1.1%	1.2%	1.1%	0.9%	1.3%	1.0%	1.6%	1.2%	1.0%	1.1%	0.22%	1.6%
	4	1.4%	1.0%	1.1%	1.2%	1.2%	1.0%	1.6%	1.2%	1.6%	1.3%	1.1%	1.3%	0.22%	1.6%
	5	1.3%	0.9%	1.1%	1.2%	1.1%	1.0%	1.5%	1.1%	1.6%	1.3%	1.0%	1.2%	0.21%	1.6%
2	1	0.2%	0.2%	0.2%	0.1%	0.2%	0.2%	0.2%	0.2%	0.1%	0.2%	0.1%	0.2%	0.03%	0.2%
	2	0.5%	0.4%	0.5%	0.4%	0.4%	0.5%	0.6%	0.5%	0.4%	0.5%	0.4%	0.5%	0.06%	0.6%
	3	0.7%	0.7%	0.7%	0.7%	0.6%	0.7%	0.9%	0.7%	0.6%	0.8%	0.6%	0.7%	0.07%	0.9%
	4	0.8%	0.7%	0.8%	0.8%	0.7%	0.8%	0.9%	0.8%	0.7%	0.8%	0.7%	0.8%	0.07%	0.9%
	5	0.7%	0.7%	0.8%	0.7%	0.6%	0.8%	0.8%	0.7%	0.6%	0.7%	0.7%	0.7%	0.06%	0.8%
3	1	0.0%	0.0%	0.0%	0.0%	0.0%	0.0%	0.0%	0.0%	0.0%	0.0%	0.0%	0.0%	0.00%	0.0%
	2	0.3%	0.2%	0.2%	0.2%	0.1%	0.3%	0.2%	0.3%	0.5%	0.1%	0.2%	0.2%	0.10%	0.5%
	3	0.3%	0.2%	0.2%	0.2%	0.2%	0.3%	0.2%	0.3%	0.5%	0.1%	0.2%	0.2%	0.10%	0.5%
	4	0.3%	0.2%	0.2%	0.2%	0.2%	0.3%	0.2%	0.3%	0.5%	0.2%	0.2%	0.2%	0.10%	0.5%
	5	0.3%	0.2%	0.2%	0.2%	0.2%	0.3%	0.2%	0.3%	0.5%	0.2%	0.2%	0.2%	0.09%	0.5%

Note: Model 1 = standard fixed-base baseline (Risk Category II); Model 2 = stiffened fixed-base (Risk Category IV); Model 3 = base-isolated (utilizing the Model 1 superstructure). All time history analyses were evaluated at the Maximum Considered Earthquake (MCE_R) demand level. Time History representations: 1 = 2844986-Valdivia; 2 = Tohoku-41211; 3 = Iwate-off-Kazuno; 4 = Ki se-Atsumi; 5 = Northridge-02-Anaverde Valley - City R; 6 = Northwest China-02-Jiashi; 7 = Chi Chi-Taiwan-02-CHY025; 8 = Northern Calif-01-Ferndale City Hall; 9 = Friuli-Italy-02-Codroipo; 10 = Coyote Lake-Halls Valley; 11 = Victoria Mexico-Sahop Casa Flores. IO = Immediate Occupancy; LS = Life Safety; CP = Collapse Prevention. $\bar{x}$ *= mean; s = standard deviation;* $x_{\max}$ *= maximum value.*

4.4 Floor Acceleration Responses

Fig. 16 and Table 13 compare the peak floor accelerations across the models. The dashed line represents a 0.22g floor-level acceleration demand indicator for server areas, rather than a direct safety limit for individual hardware components, which were not explicitly modeled in this global analysis. Model 2 experiences an average 25% amplification in roof acceleration relative to Model 1. However, Model 3 achieves a 71% average reduction in roof acceleration, consistently maintaining values below the 0.22g threshold across all floors housing server data racks (stories 1 to 4). As illustrated in Fig. 5b, the roof level (story 5) is used for mechanical equipment areas and does not contain data racks.

Table 13. Summary of floor acceleration responses (g)

		Time History													
Model	Story	1	2	3	4	5	6	7	8	9	10	11	$\bar{x}$	s	$x_{\max}$
1	1	0.46	0.47	0.42	0.47	0.4	0.49	0.48	0.46	0.4	0.45	0.46	**0.45**	**0.03**	**0.49**
	2	0.66	0.55	0.53	0.59	0.48	0.68	0.52	0.47	0.54	0.64	0.52	**0.56**	**0.07**	**0.68**
	3	0.73	0.56	0.56	0.71	0.56	0.65	0.57	0.5	0.58	0.61	0.5	**0.59**	**0.08**	**0.73**
	4	0.46	0.48	0.4	0.6	0.49	0.56	0.45	0.5	0.49	0.59	0.47	**0.5**	**0.06**	**0.6**
	5	0.71	0.74	0.7	0.96	0.78	0.79	0.77	0.69	0.68	0.72	0.93	**0.77**	**0.09**	**0.96**
2	1	0.43	0.42	0.41	0.4	0.39	0.43	0.46	0.38	0.41	0.47	0.48	**0.43**	**0.03**	**0.48**
	2	0.49	0.53	0.51	0.58	0.73	0.54	0.53	0.68	0.58	0.74	0.66	**0.6**	**0.09**	**0.74**
	3	0.61	0.59	0.77	0.69	0.71	0.61	0.64	0.81	0.71	0.86	0.66	**0.7**	**0.09**	**0.86**
	4	0.62	0.69	0.7	0.66	0.7	0.75	0.69	0.75	0.71	0.75	0.78	**0.71**	**0.05**	**0.78**
	5	1.01	1.08	1.02	0.94	1.2	1.01	1.02	0.96	1.07	1.03	1.02	**1.03**	**0.07**	**1.2**
3	1	0.16	0.15	0.15	0.15	0.13	0.1	0.19	0.2	0.21	0.13	0.09	**0.15**	**0.04**	**0.21**
	2	0.16	0.19	0.21	0.19	0.15	0.13	0.16	0.12	0.1	0.13	0.12	**0.15**	**0.03**	**0.21**
	3	0.18	0.14	0.14	0.17	0.15	0.11	0.16	0.1	0.11	0.14	0.11	**0.14**	**0.03**	**0.18**
	4	0.14	0.13	0.11	0.15	0.11	0.12	0.12	0.1	0.08	0.13	0.1	**0.12**	**0.02**	**0.15**
	5	0.28	0.17	0.18	0.19	0.23	0.21	0.19	0.16	0.11	0.21	0.14	**0.19**	**0.05**	**0.28**

Note: Model 1 = standard fixed-base baseline (Risk Category II); Model 2 = stiffened fixed-base (Risk Category IV); Model 3 = base-isolated (utilizing the Model 1 superstructure). All time history analyses were evaluated at the Maximum Considered Earthquake (MCE_R) demand level. Time History representations: 1 = 2844986-Valdivia; 2 = Tohoku-41211; 3 = Iwate-off-Kazuno; 4 = Ki se-Atsumi; 5 = Northridge-02-Anaverde Valley - City R; 6 = Northwest China-02-Jiashi; 7 = Chi Chi-Taiwan-02-CHY025; 8 = Northern Calif-01-Ferndale City Hall; 9 = Friuli-Italy-02-Codroipo; 10 = Coyote Lake-Halls Valley; 11 = Victoria Mexico-Sahop Casa Flores. $\bar{x}$ *= mean; s = standard deviation;* $x_{\max}$ *= maximum value.*

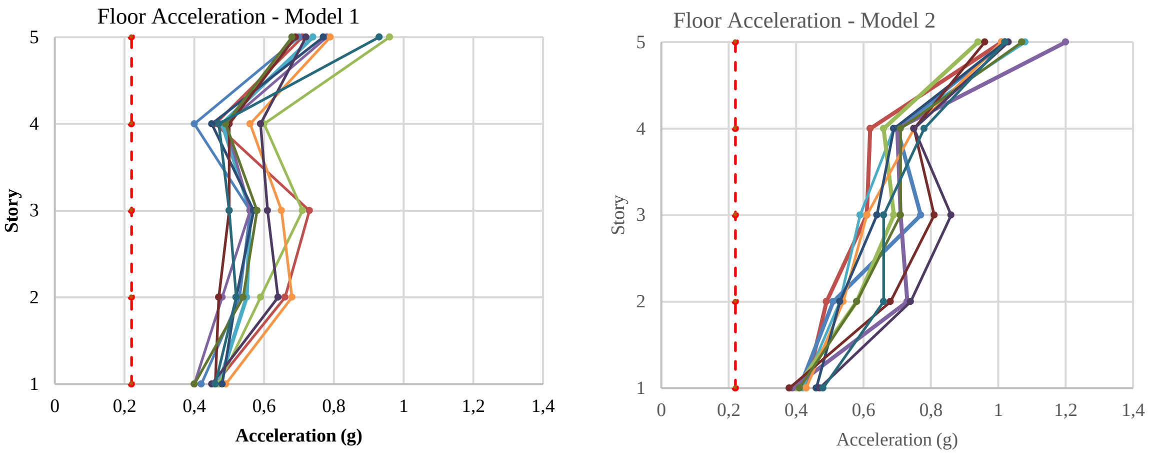

(a) Model 1

(b)Model 2

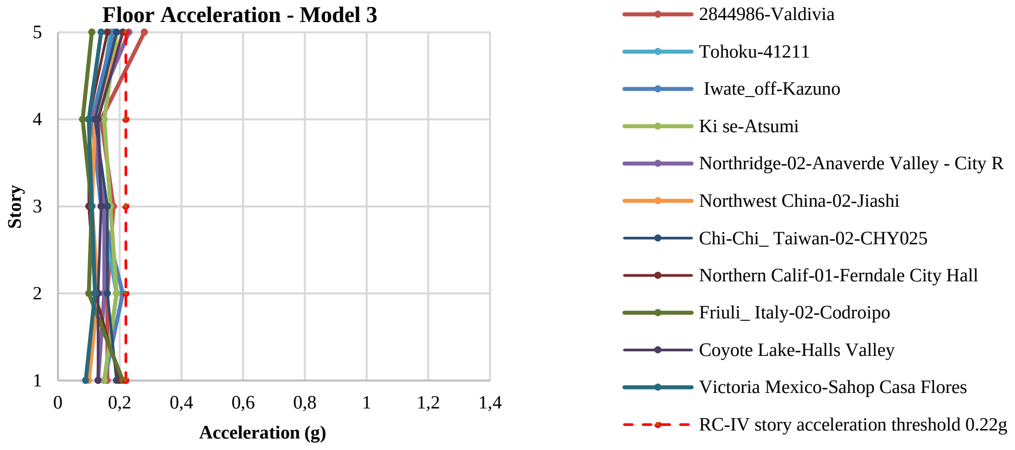

(c) Model 3

Fig. 16. Floor acceleration responses across story levels under MCE$_R$ ground motions: (a) Model 1 (standard fixed-base baseline for Risk Category II); (b) Model 2 (stiffened fixed-base for Risk Category IV); (c) Model 3 (base-isolated utilizing the Model 1 superstructure). The red dashed line represents the 0.22g floor-level acceleration demand indicator for server areas

4.5 Uplift Prevention

In the design of friction pendulum isolation systems, the occurrence of uplift (separation of the slider from the concave surface) is prohibited, as standard isolator devices are not designed to resist tensile forces. Following the methodology established by Imran et al. [14], this study utilizes the monitoring of vertical deformation at the isolation interface as a proxy to verify the absence of tensile reactions. Under this convention, negative vertical deformation values indicate downward displacement (compression), while positive values indicate uplift. The results of this verification, summarized in Table 14, confirm that vertical deformations for all DCFP units remained negative (compressive) across all ground motions, indicating no uplift occurred.

4.6 Base Isolation Hysteretic Curve

Fig. 17 illustrates the force-displacement hysteresis loops of the base isolation system under the selected MCE$_R$ ground motions. The hysteresis loops reflect the damping force generated by the combined mechanics of sliding friction and the pendulum's motion. As shown in the graph, the force demands across all eleven earthquake records remain within the maximum capacity of the device (indicated by the dashed envelope). This confirms that the selected isolation units are appropriately sized to safely accommodate the target MCE$_R$ seismic hazard.

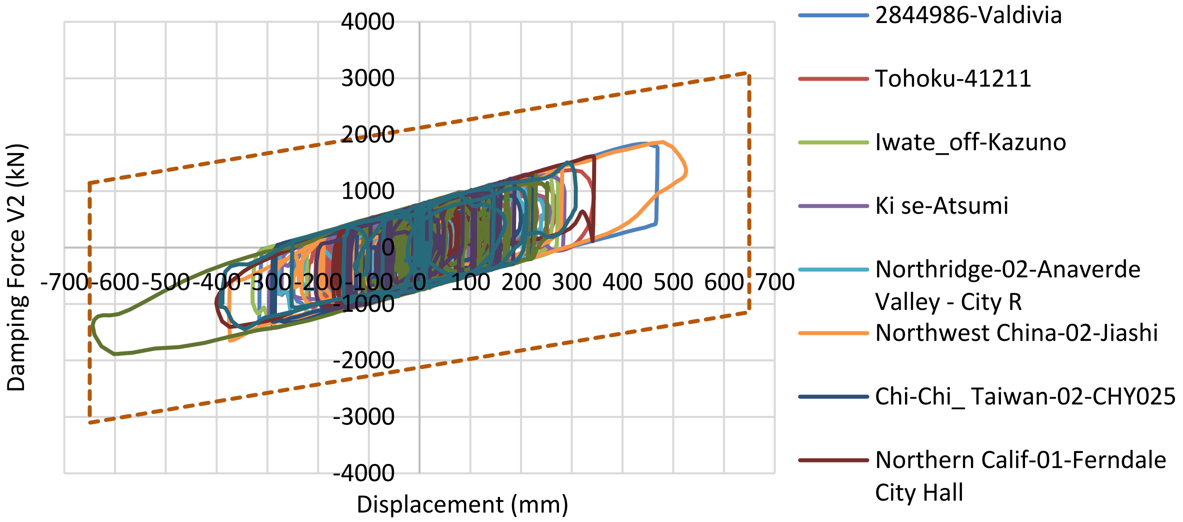

Fig. 17. Force-displacement hysteresis loops of the Double Concave Friction Pendulum (DCFP) system for Model 3 under selected MCE_R ground motions. The outer dashed envelope denotes the maximum damping force capacity of the device, defining the reference boundary for the hysteretic response.

Table 14. Summary of vertical deformations at the isolation interface

Ground Motion Data	Model 3 Vertical Deformation (mm)
2844986-Valdivia	-0.182
Tohoku-41211	-0.180
Iwate_off-Kazuno	-0.162
Ki se-Atsumi	-0.088
Northridge-02-Anaverde Valley - City R	-0.153
Northwest China-02-Jiashi	-0.177
Chi-Chi_ Taiwan-02-CHY025	-0.15
Northern Calif-01-Ferndale City Hall	-0.149
Friuli_ Italy-02-Codroipo	-0.154
Coyote Lake-Halls Valley	-0.146
Victoria Mexico-Sahop Casa Flores	-0.180

4.7 Discussion

This subsection interprets the results in the context of data center operational requirements and compares findings with established literature.

4.7.1 Effectiveness of Base Isolation Against Conventional Strengthening

The results highlight a critical limitation of conventional strengthening. While the added stiffness (Model 2, I_e = 1.5) successfully controlled structural drift (Fig. 15 and Table 12), it inherently induced higher seismic forces. This resulted in a 6% increase in mean total base shear compared to the baseline Model 1. This increase is governed by fundamental structural dynamics. The additional stiffness in Model 2 decreased the building's natural period. As a result, the structure attracted higher spectral accelerations from the ground motion, leading to the observed amplification in base shear. Furthermore, Model 2 could only deliver a Life Safety (LS) performance level, as it still experienced localized yielding within its shear wall elements. Although this performance satisfies the minimum ASCE 7 and SNI 1726 requirements for Risk Category IV buildings under MCER ground motions, Model 2 fails to meet the TIA-942B provision for a minimum Immediate Occupancy performance level.

In contrast, the base isolation system (Model 3) effectively decoupled the superstructure, maintaining it at the Immediate Occupancy performance level (Fig. 11–Fig. 13 and Table 8–Table

10). This configuration achieved a 67% average reduction in total base shear. Regarding inelastic deformation, only the isolated Model 3 successfully maintained all columns and shear walls in a fully elastic state (A-B range), while limiting minor yielding (Immediate Occupancy, IO) to an average of 3% in the beam elements.

4.7.2 Criticality of Peak Floor Acceleration Control for Operational Continuity

Data centers require peak floor accelerations to be maintained below the 0.22g threshold [8], which represents a critical floor-level demand indicator for server areas to mitigate the risk of physical damage and disruption to data stored in hard disk drives (HDDs). Consistent with the findings of Erkus et al. [1], the conventional fixed-base models in this study failed to satisfy this threshold. The simulation of a multi-story facility captured the influence of higher vibration modes, revealing a significant amplification of floor accelerations at higher elevations. Conventional code-compliant stiffening magnifies this issue. Model 2, which was designed with increased lateral stiffness to meet drift limits, amplified maximum floor accelerations by up to 25% compared to the baseline (Model 1). From a structural dynamic's standpoint, increasing the lateral stiffness inherently shortens the fundamental period of the building, thereby shifting the structure into a higher spectral acceleration region on the response spectrum. Additionally, the stiffer frame increased the participation of higher vibration modes, which further amplified the floor acceleration demands at the upper server floors (Stories 1–4).

The DCFP base isolation system implemented in Model 3 directly mitigated this phenomenon by lengthening the fundamental period to 4.9 s and effectively decoupling the superstructure from the ground motion. The NLTHA results confirmed this theoretical behavior. The isolated model experienced predominantly rigid body motion with inter-story drifts averaging 0.2%, maintaining a uniform and low floor acceleration profile across all server floors (Stories 1–4), and effectively limiting maximum floor accelerations below the 0.22g threshold. While the overall effectiveness of the FPS observed here aligns with existing literature [10,13–15,17–19], the 67% reduction in total base shear was notably higher than the ranges typically reported for standard buildings (e.g., [14]). This difference was attributed to the higher performance targets of the design. To satisfy the 0.22g floor acceleration demand, the isolation system required a long period (4.9 s) and a large effective radius of curvature (R_{eq} = 6000 mm).

5. Conclusions

This study evaluated the seismic performance of a multi-story data center using Nonlinear Time History Analysis (NLTHA) under MCE$_R$ ground motions. The evaluated results are limited to the analyzed structural configurations, the DCFP properties, the selected ground motions, and the underlying numerical assumptions. By comparing a standard fixed-base frame (Model 1), a stiffened Risk Category IV frame (Model 2), and a base-isolated structure (Model 3), the following conclusions are drawn:

- Structural Component Performance: The base-isolated structure (Model 3) maintained all plastic hinges within the Operational to Immediate Occupancy (A-IO) range. Conversely, the baseline structure (Model 1) experienced severe yielding, reaching Life Safety to Collapse Prevention (LS-CP) levels, while the stiffened structure (Model 2) sustained moderate damage (IO-LS). Although Model 2 complies with the ASCE 7 and SNI 1726 provisions for Risk Category IV buildings under MCER demands, it fails to meet the minimum Immediate Occupancy targets required by the TIA-942 standard. Consequently, among the evaluated configurations, Model 3 satisfies the structural component performance criteria of both the ASCE 7 and SNI 1726 building codes for essential facilities and the TIA-942 standard.
- Total Base Shear Response: The isolation system in Model 3 reduced the average total base shear by 67% compared to the baseline (Model 1). In contrast, the conventional stiffening method applied in Model 2 increased the total base shear demand by 6% due to the added structural stiffness.
- Drift Control: Model 3 experienced inter-story drifts averaging 0.2%, indicating rigid body motion of the superstructure. While the stiffened structure (Model 2) kept drifts below the

1% limit prescribed for Risk Category IV buildings under MCE_R demands, the baseline (Model 1) exceeded this allowable threshold.

- Floor Acceleration Response: The responses of both fixed-base models exceeded the 0.22g floor acceleration threshold under MCE_R events. Stiffening the structure (Model 2) amplified these floor acceleration responses compared to the baseline (Model 1). Within the limits of the analyzed structural configuration, DCFP properties, selected ground motions, and numerical assumptions, the implementation of base isolation in Model 3 successfully maintained the floor accelerations below the 0.22g threshold across Stories 1–4, where the server racks are installed.

5.1 Limitations

This study assumes a regular structural configuration adhering to SNI 1726 [3] and ASCE 7 [2]. Effects of significant structural irregularities, near-fault directivity, and vertical ground motion components were excluded and warrant future investigation for specific site contexts.

Acknowledgements

The authors gratefully acknowledge Tri Suryadi, Technical Advisor at Freyssinet Indonesia, for his valuable support and insightful discussions throughout the course of this study.

References

[1] Erkus B, Polat SS, Darama H. Seismic design of data centers for tier III and tier IV resilience: Project examples. In: 11th National Conference on Earthquake Engineering 2018, NCEE 2018: Integrating Science, Engineering, and Policy. 2018. p. 922–32.
[2] American Society of Civil Engineers. Minimum design loads and associated criteria for buildings and other structures (ASCE/SEI 7-22). Reston, VA: American Society of Civil Engineers; 2022. https://doi.org/10.1061/9780784415788.
[3] Badan Standardisasi Nasional. Earthquake resistance design procedures for building and non-building structures (Tata cara perencanaan ketahanan gempa untuk struktur bangunan gedung dan non gedung) (SNI 1726:2019). Jakarta: Badan Standardisasi Nasional; 2019.
[4] Telecommunications Industry Association. Telecommunications infrastructure standard for data centers (TIA-942-B). Arlington, VA: Telecommunications Industry Association; 2017.
[5] Horison. Tiered storage optimization [Internet]. 2025 [cited 2026 Jun 12]. Available from: https://horison.com/wp-content/uploads/2021/11/Fujifilm-Tiered-Storage-2021.pdf
[6] Khan AQ, Matskin M, Prodan R, Bussler C, Roman D, Soylu A. Cloud storage tier optimization through storage object classification. Computing. 2024;106:3389–418. https://doi.org/10.1007/s00607-024-01281-2.
[7] Alhan C, Gavin HP. Reliability of base isolation for the protection of critical equipment from earthquake hazards. Eng Struct. 2005;27:1435–49. https://doi.org/10.1016/j.engstruct.2005.04.007.
[8] Seagate. Seagate® kinetic HDD product manual [Internet]. 2015 [cited 2026 Jun 12]. Available from: https://www.seagate.com/www-content/product-content/hdd-fam/kinetic-hdd/en-us/docs/100764174b.pdf
[9] Constantinou MC, Soong TT, Dargush GF. Passive energy dissipation systems for structural design and retrofit. Reston, VA: American Society of Civil Engineers; 1998.
[10] Fenz DM, Constantinou MC. Behaviour of the double concave friction pendulum bearing. Earthq Eng Struct Dyn. 2006;35:1403–24. https://doi.org/10.1002/eqe.589.
[11] He P, Ma Y, Liu C. Seismic resilience assessment of base-isolated structures with friction pendulum isolation bearings based on two-dimensional fragility. J Build Eng. 2025;103:112202. https://doi.org/10.1016/j.jobe.2025.112202.
[12] He Q, Ling K, Zhao G, Li X, Liu D, Yao S, et al. Seismic response analysis of overall friction pendulum bearing (OFPB) isolated structures. Structures. 2024;68:107224. https://doi.org/10.1016/j.istruc.2024.107224.
[13] Buckle IG, Mayes RL. Seismic isolation: history, application, and performance-a world view. Earthq Spectra. 1990;6:161–201.
[14] Imran I, Siringoringo DM, Michael J. Seismic performance of reinforced concrete buildings with double concave friction pendulum base isolation system. Structures. 2021;34:462–78. https://doi.org/10.1016/j.istruc.2021.07.084.

[15] Kasai K, Mita A, Kitamura H, Matsuda K, Morgan TA, Taylor AW. Performance of seismic protection technologies during the 2011 Tohoku-oki earthquake. Earthq Spectra. 2013;29:265–93. https://doi.org/10.1193/1.4000131.

[16] Pan P, Zamfirescu D, Nakashima M, Nakayasu N, Kashiwa H. Base isolation design practice in Japan: introduction to the post-Kobe approach. J Earthq Eng. 2005;9:147–71. https://doi.org/10.1080/13632460509350537.

[17] Ponzo FC, Di Cesare A, Telesca A, Pavese A, Furinghetti M. Advanced modelling and risk analysis of RC buildings with sliding isolation systems designed by the Italian seismic code. Appl Sci. 2021;11:1938. https://doi.org/10.3390/app11041938.

[18] Tsai HC, Kelly JM. Seismic response of the superstructure and attached equipment in a base-isolated building. Earthq Eng Struct Dyn. 1989;18:551–64. https://doi.org/10.1002/eqe.4290180409.

[19] Zayas VA, Low SS, Mahin SA. A simple pendulum technique for achieving seismic isolation. Earthq Spectra. 1990;6:317–33. https://doi.org/10.1193/1.1585573.

[20] Vibhute AS, Bharti SD, Shrimali MK, Datta TK. Performance evaluation of FPS and LRB isolated frames under main and aftershocks of an earthquake. Structures. 2022;44:1532–45. https://doi.org/10.1016/j.istruc.2022.08.082.

[21] Chen P, Wang B, Zhang Z, Li T, Dai K. A generalized model of lead rubber bearing considering large strain stiffening and degradation. Eng Struct. 2023;275:115264. https://doi.org/10.1016/j.engstruct.2022.115264.

[22] Computers and Structures, Inc. ETABS. Version 19.1.0. Berkeley, CA: Computers and Structures, Inc.; 2019.

[23] Badan Standardisasi Nasional. Minimum design loads and related criteria for buildings and structures (Beban desain minimum dan kriteria terkait untuk bangunan gedung dan struktur) (SNI 1727:2020). Jakarta: Badan Standardisasi Nasional; 2020.

[24] PusGen. Map of indonesia's earthquake sources and hazards in 2024 (Peta sumber dan bahaya gempa indonesia tahun 2024). 2024.

[25] PusGen. Earthquake hazard deaggregation map for earthquake resistant infrastructure planning and evaluation (Peta deagregasi bahaya gempa untuk perencanaan dan evaluasi infrastruktur tahan gempa). 2022.

[26] Hilber HM, Hughes TJR, Taylor RL. Improved numerical dissipation for time integration algorithms in structural dynamics. Earthq Eng Struct Dyn. 1977;5:283–92. https://doi.org/10.1002/eqe.4290050306.

[27] Mander JB, Priestley MJN, Park R. Theoretical stress-strain model for confined concrete. J Struct Eng. 1988;114:1804–26. https://doi.org/10.1061/(ASCE)0733-9445(1988)114:8(1804).

[28] Ziegler H. A modification of Prager's hardening rule. Q Appl Math. 1959;17:55–65. https://doi.org/10.1090/qam/104405.

[29] American Society of Civil Engineers. Seismic evaluation and retrofit of existing buildings (ASCE/SEI 41-17). Reston, VA: American Society of Civil Engineers; 2017. https://doi.org/10.1061/9780784414859.

[30] Freyssinet. ISOSISM® PS pendulum systems. 2024. https://www.freyssinet.com/solution/build/seismic-protection/isosism-isolation-systems/ (accessed June 12, 2026).

[31] Freyssinet. ISOGLIDE technical data sheet reference no.: FT En CV 4 1 1 [Internet]. 2018 [cited 2026 Jun 12]. Available from: https://www.freyssinet.cz/gallery/c_v_1_3_1_ft_isoglide__en_v04_-comparation_isoglide_x_uhmwpe_(01-2022).pdf

Appendix 1 Structure Elements Detail

Table 15. Beam schedule of Model 1.

Beam-ID	Beam Size (*B* x *H*)	Top Bar End	Bot Bar End	Mid Top Bar	Mid Bot Bar	Trv End Bar	Trv Mid Bar	Side Bar (Torsion Bar)
B1	400x800	5-D25 + 5-D22	4-D22	2-D22 + 2-D19	4-D25 + 2-D22	4 - D-10-150	3 - D-10-200	6-D19
B1-1	400x900	5-D29 + 5-D25	5-D22	3-D25	5-D29	3 - D-10-150	3 - D-10-200	6-D19
B1-2	400x900	5-D25 + 5-D29	4-D25	4-D25	4-D25 + 4-D25	4 - D-13-150	2 - D-13-200	6-D19
B2	400x800	5-D29 + 6-D25	4-D25	3-D29	4-D29 + 4-D25	3 - D-13-130	2 - D-13-150	6-D19
B2-1	500x900	6-D29 + 5-D29	4-D29	4-D25	5-D25 + 4-D29	3 - D-13-120	3 - D-13-220	8-D19
B2-2	500x1000	5-D29 + 5-D25	4-D25	4-D25	5-D29 + 4-D29	4 - D-13-150	2 - D-13-200	6-D22
B2-3	500x1000	5-D29 + 5-D29	4-D29	4-D25	5-D25 + 4-D25	4 - D-13-150	3 - D-13-200	6-D19
B4	400x1100	5-D22 + 4-D16	5-D22	5-D22	5-D22	3 - D-10-150	3 - D-10-180	12-D25
B4-1	400x1100	5-D22 + 5-D16	5-D22	5-D22	5-D22	4 - D-10-120	4 - D-10-200	12-D25
B5	400x1100	5-D25 + 5-D16	5-D22	5-D22	5-D22	3 - D-10-150	3 - D-10-170	12-D25
B5-1	400x1100	4-D25 + 4-D25	5-D22	5-D22	5-D22	4 - D-10-100	4 - D-10-200	12-D25
B3	400x700	5-D16	5-D16	5-D16	4-D29 + 4-D22	3 - D-10-200	3 - D-10-200	6-D16

Note: B = beam width; H = beam depth; Bot = bottom; Mid = middle; Trv = transversal; D = deformed reinforcing bar diameter. All dimensions are in millimeters (mm) unless otherwise specified.

Table 16. Column schedule of Model 1

Column-ID	Column Size (*B* x *H*)	End Long Bar	Mid Long Bar	Trv End Bar	Ties at End Section	Trv Mid Bar	Ties at Mid-Section
C0	1000x1000	1 x 28-D29 + 1 x 28-D25	1 x 28-D29 + 1 x 28-D25	D10-150	6 - D10-150	D10-250	3 - D10-250
C1	800x800	2 x 20-D25	2 x 20-D25	D13-140	6 - D13-140	D10-150	3 - D10-150

Note: B = column width; H = column depth; Long = longitudinal; Mid = middle; Trv = transversal; D = deformed reinforcing bar diameter. All dimensions are in millimeters (mm) unless otherwise specified.

Table 17. Shear wall schedule of Model 1

Wall-ID	Total Length (m)	Web					Boundary Element				
		Thk (mm)	Number of Layers	Ver Bar	Hor Bar	Ties	Length (m)	Thk (mm)	Ver Bar	Hor Bar	Ties
W0	10	600	2	D-32-100	D-22-150	4-D-22-150	2000	600	D-32-100	D-22-100	13-D-22-100
W1	10	400	2	D-29-150	D-16-150	4-D-13-100	1750	400	D-29-100	D-16-150	12-D-16-150

Note: Thk = thickness; Ver = vertical; Hor = horizontal; D = deformed reinforcing bar diameter.

Table 18. Beam schedule of Model 2.

Beam-ID	Beam Size (*B* x *H*)	Top Bar End	Bot Bar End	Mid Top Bar	Mid Bot Bar	Trv End Bar	Trv Mid Bar	Side Bar (Torsion Bar)
B1	500x900	5-D32 + 5-D29	6-D36	4-D25	7-D25	3 - D-10-100	2 - D-10-150	6-D19
B1-1	500x1000	6-D32 + 6-D29	6-D36	3-D29	4-D29	3 - D-10-120	3 - D-10-120	6-D19
B1-2	500x1000	6-D36 + 5-D36	6-D36	4-D25	4-D29 + 4-D29	4 - D-10-150	4 - D-10-200	6-D25
B2	500x900	6-D36 + 6-D36	6-D36	5-D25	5-D25 + 4-D25	4 - D-13-150	3 - D-13-200	8-D22
B2-1	500x1000	6-D32 + 6-D29	6-D36	4-D25	5-D29 + 4-D29	4 - D-13-120	3 - D-13-250	6-D22
B2-2	500x1000	6-D32 + 5-D25	6-D36	4-D25	4-D29 + 4-D25	4 - D-13-120	3 - D-13-200	8-D29
B2-3	500x1000	6-D36 + 5-D32	6-D36	5-D25	5-D29 + 4-D29	4 - D-13-150	4 - D-13-250	14-D25
B4	600x1200	7-D32 + 6-D29	6-D36	4-D29	5-D29 + 3-D25	4 - D-13-150	4 - D-13-150	12-D32
B5	600x1200	7-D32 + 5-D32	6-D36	4-D29	4-D32 + 3-D29	4 - D-13-150	4 - D-13-200	13-D32
B5-1	600x1200	6-D36 + 6-D29	6-D36	4-D29	5-D32	4 - D-10-120	4 - D-10-120	10-D32
B3	400x700	5-D22	5-D22	5-D16	4-D25	3 - D-10-150	3 - D-10-150	6-D16

Note: B = beam width; H = beam depth; Bot = bottom; Mid = middle; Trv = transversal; D = deformed reinforcing bar diameter. All dimensions are in millimeters (mm) unless otherwise specified.

Table 19. Column schedule of Model 2.

Column	Column Size (*B* x *H*)	End Longitudinal Bar	Mid Long Bar	Trv End Bar	Ties at End Section	Trv Mid Bar	Ties at Mid-Section
C0	1250x1250	2 x 40-D32	2 x 40-D32	D13-100	9 - D13- 100	D10-280	4 - D10-280
C1	800x800	2 x 32-D29	2 x 32-D29	D10-100	6 - D10- 100	D10-250	2 - D10-250

Note: B = column width; H = column depth; Long = longitudinal; Mid = middle; Trv = transversal; D = deformed reinforcing bar diameter. All dimensions are in millimeters (mm) unless otherwise specified.

Table 20. Shear wall schedule of Model 2

Wall-ID	Total Length (m)	Web					Boundary Element				
		Thk (mm)	Number of Layers	Ver Bar	Hor Bar	Ties	Length (m)	Thk (mm)	Ver Bar	Hor Bar	Ties
W0	10	700	2	D-32-100	D-22-150	4-D-22-150	3300	700	D-32-100	D-22-100	20-D-22-100
W1	10	500	2	D-29-150	D-22-150	4-D-13-100	2500	400	D-29-100	D-22-150	20-D-22-150

Note: Thk = thickness; Ver = vertical; Hor = horizontal; D = Deformed reinforcing bar diameter.